Last edited: March 28, 2007
Preprint typeset using LaTeX style emulateapj v. 2/14/03

THE STELLAR MASS ASSEMBLY OF GALAXIES FROM Z=0 TO Z=4. ANALYSIS OF A SAMPLE SELECTED IN THE REST-FRAME NEAR-INFRARED WITH SPITZER

Pablo G. Pérez-González[1,2], George H. Rieke[3], Victor Villar[1], Guillermo Barro[1], Myra Blaylock[3], Eiichi Egami[3], Jesús Gallego[1], Armando Gil de Paz[1], Sergio Pascual[1], Jaime Zamorano[1]

Last edited: March 28, 2007

ABSTRACT

Using a sample of ∼28,000 sources selected at 3.6–4.5 microns using *Spitzer* observations of the Hubble Deep Field North, the Chandra Deep Field South, and the Lockman Hole (for a total surveyed area of ∼664 arcmin^2), we study the evolution of the stellar mass content of the Universe from z=0 to z=4 (in the last 12 Gyr). We calculate stellar masses and photometric redshifts, based on a set of ∼2,000 templates built with stellar population and dust emission models fitting the ultraviolet to mid-infrared spectral energy distributions of galaxies with measured spectroscopic redshifts. We estimate stellar mass functions for different redshift intervals. We find that 50% of the local stellar mass density was assembled at 0<z<1 (at an average rate of 0.036 $\mathcal{M}_\odot$yr^{-1}), and at least another 40% at 1<z<4 (at an average rate of 0.054 $\mathcal{M}_\odot$yr^{-1}). Our results confirm and quantify the "downsizing" scenario of galaxy formation. We find that the most massive galaxies ($\mathcal{M}>10^{12.0}$ $\mathcal{M}_\odot$) assembled the bulk of their stellar content rapidly (in 1-2 Gyr) beyond z= 3 in very intense star formation events (producing high specific star formation rates). Galaxies with $10^{11.5}<\mathcal{M}<10^{12.0}$ $\mathcal{M}_\odot$ assembled half of their stellar mass before z∼1.5, and more than 90% of their mass was already in place at z∼0.6. Galaxies with $\mathcal{M}<10^{11.5}$ $\mathcal{M}_\odot$ evolved more slowly (presenting smaller specific star formation rates), assembling half of their stellar mass before z∼1. These galaxies experienced another significant increase in their stellar mass at low redshift: about 40% of the local stellar mass density of $10^{9.0}<\mathcal{M}<10^{11.0}$ $\mathcal{M}_\odot$ galaxies was assembled below z∼0.4, most probably through accretion of small satellites producing little star formation. The cosmic stellar mass density at z>2.5 is dominated by optically faint ($R\gtrsim25$) red galaxies (Distant Red Galaxies or BzK sources) which account for ∼30% of the global population of galaxies, but contribute with more than 60% to the cosmic stellar mass density. Bluer galaxies (e.g., Lyman Break Galaxies) are more numerous but less massive, contributing with less than 50% to the global stellar mass density at high redshift.

Subject headings: galaxies: evolution — galaxies: starburst — galaxies: photometry — galaxies: high-redshift — infrared: galaxies

1. INTRODUCTION

In the last decade, our knowledge about the formation and evolution of galaxies has increased significantly with the advent of deep and/or wide photometric and spectroscopic galaxy surveys carried out at different wavelengths. This advance in our understanding of the evolution of the Universe is succinctly represented in the so-called Lilly-Madau plot (Lilly et al. 1996; Madau et al. 1996), a diagram showing the evolution of the Star Formation Rate (SFR) density of the Universe as a function of look-back time (or redshift). Originally, with only a few points in the diagram, it was clearly visible that in the last ∼8 Gyr (i.e., about 55% of its age) the Universe experienced a significant decrease (of about a factor of 10) in the rate at which new stars were created. Nowadays, there are more than 80 data points in the Lilly-Madau diagram (see Hopkins 2004 for a nice compilation of results on this topic; see also Schiminovich et al. 2005, Pérez-González et al. 2005, and Hopkins & Beacom 2006), and the picture is clearer at $z\lesssim1$, where there is just a factor of 2 scatter among the estimations coming from different surveys, and using different selection techniques and SFR tracers. At $z\gtrsim1$, the uncertainties are larger, up to a factor of ∼5, but there is increasing evidence that the SFR density remained approximately constant for 4–5 Gyr (from z∼1 to z∼4).

Although the Lilly-Madau plot concentrates a large amount of information about the formation of structures in the Universe, the (recent) SFR is not the best parameter to characterize a galaxy. Indeed, the stellar mass or the metallicity, which are closely linked to the star formation history, are more appropriate parameters to follow the evolution of galaxies. Thus, an increasing number of studies explore the evolution of the cosmic comoving stellar mass density, showing that it has steadily increased in the last 12 Gyr (see, e.g., Brinchmann & Ellis 2000, Dickinson et al. 2003b, Glazebrook et al. 2004, Drory et al. 2005, Fontana et al. 2006; see also the references given in Figure 7).

Because of the increasingly large scale of cosmological surveys, the problem of the evolution of galaxies is now being addressed by dividing the samples into ranges in stellar mass. In this context, the evolution of galaxies seems to follow a 'downsizing' scenario (Cowie et al. 1996), where the most massive galaxies are formed first in violent episodes of star formation (with high specific SFRs, i.e., high values of the SFR per unit stellar mass) and the star formation continues in less massive systems

[1] Departamento de Astrofísica, Facultad de CC. Físicas, Universidad Complutense de Madrid, E-28040 Madrid, Spain
[2] Associate Astronomer at Steward Observatory, The University of Arizona
[3] The University of Arizona, Steward Observatory, 933 N Cherry Avenue, Tucson, AZ 85721

until more recent epochs (Bauer et al. 2005; Bundy et al. 2006; Heavens et al. 2004; Juneau et al. 2005; Pérez-González et al. 2005; Tresse et al. 2006). Although the 'downsizing' picture is being confirmed by an increasing number of works, the quantification of the process is still very limited, given the necessity of large samples of high redshift galaxies with multi-wavelength data to explore it (covering from the rest-frame ultraviolet to the near-infrared and beyond).

In contrast with these observational results, classical models of galaxy evolution assuming a Cold Dark Matter (CDM) Universe usually predict that the most massive galaxies assembled late via the coalescence of small halos that form larger ones (e.g., Baugh et al. 1998; Kauffmann et al. 1993; Somerville et al. 2001). This contradicts the observational evidence of the existence of large galaxies at high redshifts (some of them already harboring old stellar populations at those early epochs, some with significant recent star formation), detected by their unusually red colors (among others, Dey et al. 1999; Dickinson et al. 2000; Elston et al. 1988; Franx et al. 2003; Im et al. 2002) or their bright emission at sub-millimeter wavelengths (e.g., Hughes et al. 1998; Smail et al. 1997, see also Blain et al. 2002 for a review). More recent models based on a ΛCDM cosmology succeed in predicting the early formation of massive galaxies by introducing very large dust extinctions, non-standard Initial Mass Functions, and/or suppression of the star formation due to the quenching of cooling flows due to supernovae or Active Galactic Nuclei (e.g., Baugh et al. 2005; Bower et al. 2006; Cole et al. 2000; Croton et al. 2006; Granato et al. 2004; Nagamine et al. 2005a).

In this paper, we observationally characterize the build-up of the stellar mass of galaxies in the last ∼12 Gyr (almost 90% of the age of the Universe) as a function of the stellar mass of each object. This is done by estimating stellar mass functions at different redshifts. Given that we are interested in the stellar mass assembly of galaxies, it would be convenient to analyze a sample whose selection is based precisely on that parameter, the stellar mass. From studies at low and intermediate redshift, we know that the rest-frame near-infrared (NIR) emission of galaxies arises mainly from relatively old stars that usually dominate the total stellar mass of galaxies, in comparison with younger stellar populations that may contribute little to the NIR emission and stellar mass, but emit strongly at bluer wavelengths. Indeed, stellar mass estimations based (only) on photometry at wavelengths bluer than ∼600 nm are particularly troublesome because of the ability of a small population of young stars to dominate the output of a galaxy. In the red and NIR, the light is dominated by similar stellar populations, but the NIR is preferred for estimating stellar masses because of its relative immunity to extinction. In addition, NIR data is crucial to detect galaxies that are very faint in the optical (too faint for optical surveys) but may contribute significantly or even dominate the stellar mass density of the Universe at high-z (e.g., Extremely Red Objects, EROs, Elston et al. 1988, Yan et al. 2000; or Distant Red Galaxies, DRGs, Franx et al. 2003, van Dokkum et al. 2003). These galaxies are usually missed by selection techniques based on rest-frame ultraviolet colors (e.g., Lyman Break Galaxies, LBGs; Steidel et al. 2003). Therefore, a sample selected in the rest-frame NIR is the most adequate to attempt a stellar mass function analysis.

This paper is based on the analysis of a sample of galaxies at $0<z<4$ selected in 3 different fields (to minimize cosmic variance problems) at 3.6-4.5 μm with the Infrared Array Camera (IRAC, Fazio et al. 2004b) onboard of the *Spitzer* Space Telescope (Werner et al. 2004). Even at the highest redshift in the sample, the sources are still selected in the rest-frame NIR (approximately the J-band), so an IRAC selected sample uniquely constitutes a statistically complete sample in stellar mass at all redshifts up to z∼4 (to a certain lower limit based on the flux cut of the sample). In addition, the estimations of the stellar masses of our galaxies always count with a NIR band, which significantly reduces the uncertainties in the derived stellar masses (see, e.g., Fontana et al. 2006), since the relatively old stellar population contributing the most to the total stellar mass of galaxies usually dominates the emission at NIR wavelengths, and also because the NIR is relatively free of extinction effects and hence is better for estimating stellar masses than shorter wavelengths. Our sample selection constitutes an extension (in area, depth, and consequently, in the number of galaxies detected) of those used by other groups based on ground-based K-band data (e.g., Drory et al. 2004 and Fontana et al. 2004).

This paper is organized as follows: Section 2 presents the dataset and samples of galaxies used in this work. Section 3 describes the stellar population and dust emission models used to estimate photometric redshifts, stellar masses, and SFRs for all galaxies in our sample. Here, we also discuss the uncertainties in these parameters. Sections 4 and 5 discuss the main results about photometric redshifts and stellar masses. More precisely, we present stellar mass functions and densities, discussing their evolution with redshift. Section 6 divides our sample into several sub-types (such as DRGs or LBGs), and discusses the evolution of galaxies of different natures and their role on the evolution of the stellar mass density of the Universe as a whole. Section 7 analyzes the SFRs of the galaxies in our sample and the evolution of the cosmic SFR density. Finally, Section 8 summarizes the conclusions of this paper.

Throughout this paper, we use a cosmology with $H_0 = 70\ \mathrm{km\,s^{-1}\,Mpc^{-1}}$, $\Omega_M = 0.3$ and $\Lambda = 0.7$. All magnitudes refer to the AB system. The results about stellar masses assume a Salpeter (1955) universal (i.e., constant through time) initial mass function with $0.1<\mathcal{M}<100\ \mathcal{M}_\odot$ and a single power-law slope in this range.

2. DATA AND SAMPLE SELECTION

2.1. *The IRAC selected sample*

This paper analyzes the main properties of the galaxies selected by IRAC (hereafter, the IRAC selected sample), which should be close to a stellar mass selected sample up to the highest redshifts in our survey. The sample is drawn from the *Spitzer* GTO (see, e.g., Pérez-González et al. 2005) and GOODS (Dickinson et al. 2003a) IRAC and MIPS observations of the Hubble Deep Field North (HDF-N) and the Chandra Deep Field South (CDF-S), and the *Spitzer* GTO data in the Lockman Hole Field (LHF). In each field, we concentrated on a reduced sky

area with the deepest coverage by *Spitzer*, and also observed by other x-ray, UV, optical, and NIR surveys. In the HDF-N, we focused our analysis in 257 arcmin^2 centered at $\alpha = 12^h38^m56^s$, $\delta = +62°14'06''$, J2000, covering the entire GOODS ACS footprint; in the CDF-S, in 225 arcmin^2 centered at $\alpha = 03^h30^m28^s$, $\delta = -27°48'18''$, J2000, also covering the entire GOODS ACS footprint; and in the LHF, in a square are of 183 arcmin^2 centered at $\alpha = 10^h52^m47^s$, $\delta = +57°29'06''$, J2000. This adds up a total surveyed area of 664 arcmin^2.

The reduction, source extraction, and photometry of the IRAC and MIPS images were performed in the same way explained in Pérez-González et al. (2005). For the IRAC images, we detected sources separately in the 2 bluer IRAC bands (at 3.6 μm and 4.5 μm), and then merged the catalogs, removed repeated sources, and measured aperture photometry in the 4 IRAC images (fixing the positions and forcing the detection in all bands), obtaining the final integrated magnitude after applying an aperture correction based on empirical Point Spread Functions (PSFs). All the sources in the IRAC sample have measured fluxes at both 3.6 μm and 4.5 μm. For the MIPS 24 μm images, we measured integrated fluxes using PSF fits and aperture corrections.

Our IRAC selected sample is composed of 9,074 sources in the HDF-N, 9,676 in the CDF-S, and 9,149 in the LHF, for a total of 27,899 sources (i.e., 42 sources/arcmin^2). Out of these, less than 3% (700 sources) are identified as stars (see the star-galaxy separation method in Section 2 2.5). Based on simulations carried out by adding artificial sources to the IRAC images and trying to recover their detection and input flux, we estimate that our IRAC catalogs in the HDF-N and the CDF-S are 75% (90%) complete down to 1.6 μJy (5.0 μJy) at 3.6 μm, and 1.4 μJy (4.0 μJy) at 4.5 μm. For the LHF, where deep GOODS IRAC data are not available, the 75% (90%) completeness levels are 2.2 μJy (5.8 μJy) at 3.6 μm, and 2.0 μJy (4.8 μJy) at 4.5 μm. Above the 75% completeness flux limits, our sample has 7,512 galaxies (after removal of stars) in the HDF-N, 6,546 galaxies in the CDF-S, and 5,341 galaxies in the LHF, adding a total of 19,399 galaxies (29.2 sources/arcmin^2). Out of these, 6,686 (35%) galaxies are detected by MIPS at 24 μm, 3,483 (18%) above our 75% completeness level ($F(24)$=80 μJy).

The *Spitzer* data were complemented with other publicly available and proprietary photometric and spectroscopic data in the 3 fields. For the HDF-N and the CDF-S, the dataset is described in detail in Pérez-González et al. (2005). For this paper, we added in the HDF-N the JK data described in Villar et al. (2007, in preparation; with limiting magnitudes[4] J=22.4 and K=21.4), GALEX data extracted from the GALEX archive (with limiting magnitudes NUV=24.9 and FUV=25.3), and the spectroscopic redshifts published by Reddy et al. (2006a). In the CDF-S, we added an image of size $37' \times 30'$ taken in the $NB816$ filter with the Suprime-Cam instrument on Subaru (with a limiting magnitude of $NB816$=24.8), and the spectroscopic redshifts published by Vanzella et al. (2006). For the LHF field (not used in Pérez-González et al. 2005), we summarize the main characteristics of the data set, including the wavelengths, limiting magnitudes, and references for each filter in Table 1.

[4] Defined as the third quartile of the magnitude distribution of our sample.

Table 1. Characteristics of the data compiled for the Lockman Hole.

Band (1)	$\lambda_{\rm eff}$ (2)	$m_{\rm lim}$ (3)	Source (4)
IRAC-3.6	3.561	23.0	*Spitzer* GTO
IRAC-4.5	4.510	23.0	*Spitzer* GTO
IRAC-5.8	5.689	22.3	*Spitzer* GTO
IRAC-8.0	7.958	22.0	*Spitzer* GTO
MIPS-24	23.844	20.0	*Spitzer* GTO
B	0.442	26.0	Subaru Deep imaging[a]
R	0.652	25.4	Subaru Deep imaging[a]
I	0.795	25.0	Subaru Deep imaging[a]
z	0.907	24.5	Subaru Deep imaging[a]
U	0.361	23.1	ING Archive[b]
g	0.486	24.0	ING Archive[b]
i	0.767	22.3	ING Archive[b]
H	1.649	20.4	TIFKAM[c]

Note. — (1) Name of the observing band. (2) Effective wavelength (in μm) of the filter+detector. (3) Limiting AB magnitudes defined as the third quartile of the magnitude distribution of our sample. (4) Source from where the data were obtained: [a] publicly available ultra-deep optical data from the SMOKA Subaru Archive, taken with the Suprime-Cam instrument on the Subaru Telescope; [b] data obtained from the Archive of the Isaac Newton Group of Telescopes, and taken with the Wide Field Camera on the 2.5m Isaac Newton Telescope; [c] Data taken with the TIFKAM instrument on the 2.1 m Telescope at Kitt Peak National Observatory.

2.2. *Merged photometric catalog*

Aperture matched photometry in all bands was carried out using the procedure described in Pérez-González et al. (2005). Briefly, the coordinates of the IRAC detected sources are cross-correlated with each one of the UV, optical and NIR catalogs using a search radius of 2.5$''$ (roughly two pixels in the IRAC images) and starting by the deepest images. Once the source was identified in one image (for most cases, the first one), we took the Kron (1980) elliptical aperture best enclosing the entire source from this reference image, and translated it to all the other bands. The aperture was large enough to enclose the PSF profile in all UV/optical/NIR images. For IRAC and MIPS, where the PSFs are comparatively large, we assumed the integrated magnitude measured in small apertures (applying aperture corrections), as discussed at the beginning of Section 2. For GALEX data, we took the best magnitude given by SEXTRACTOR. For HST images, we picked the integrated flux of the closest source measured with SEXTRACTOR, not carrying out any aperture matching.

In some cases (for 10%-15% of the entire IRAC sample in each field), there were several UV/optical/NIR counterparts (in ground-based images) for one single IRAC source within the search radius. For these sources, we remeasured the IRAC fluxes by fixing the positions of the blended objects and deconvolving the images using the IRAC PSFs[5].

[5] Although the IRAC PSFs have FWHMs of approximately 3$''$,

Most of the IRAC selected sources are detected in our deepest Subaru images in the HDF-N: approximately 90% are detected in B, R, and/or I. In these bands, 75% of our sources are brighter than $B = 25.5$, $R = 24.9$, and $I = 24.5$. In the CDF-S, 90% of the sources are detected in the $NB816$ filter, and 75% of them are brighter than $NB816 = 24.8$. In the same field, about 70% of sources are detected in B (75% of them are brighter than $B = 25.3$), 60% in R (75% of them brighter than $R = 24.8$), and 40% in I (75% of sources brighter than $I = 23.7$). MIPS at 24 μm is able to detect about 25% of the IRAC sources (75% of them above $F(24)$=40 μJy).

A negligible fraction (not large enough to change our results significantly) within the sample of IRAC sources (less than 3%) was detected in less than 5 filters (our limit to calculate a reliable photometric redshift), all of them with fluxes below the 75% completeness level.

2.3. *The optically (I-band) selected sample*

We complemented the IRAC selected sample described in the previous sections with a sample of galaxies selected in a ground-based optical image. Our goal was to check the effect on our results of the galaxies missed by IRAC, i.e., galaxies which are relatively faint in the rest-frame NIR but can be detected in deep optical imaging. This sample of NIR-faint galaxies should allow us to probe the stellar mass functions at small masses below the IRAC detection limits (and at higher masses, where the galaxies should also be detected by IRAC).

We selected the deepest ground-based images in a band common (or similar) to the 3 fields, namely, the Subaru I-band images in the LHF and the HDF-N, and the Subaru $NB816$ image (close to an I-band image, and also very deep) in the CDF-S. Hereafter, we will refer to this sample as the I-band selected galaxies.

We concentrated our analysis of the I-band selected sample on the region covered by the other surveys, and enclosing a similar number of sources as those detected with the IRAC selection. We used an area of 101 arcmin^2 centered at $\alpha = 12^h37^m00^s$, $\delta = +62°13'30''$ (J2000) in the HDF-N, 103 $'^2$ at $\alpha = 03^h32^m28^s$ $\delta = -27°48'54''$ (J2000) in the CDF-S, and 70 $'^2$ at $\alpha = 10^h52^m48^s$ $\delta = +57°29'24''$ in the LHF. The samples are formed by 7,326 sources (112 of them identified as stars) in the HDF-N, 6,680 (87 stars) in the CDF-S, and 6,797 (99 stars) in the LHF, for a total of 20,505 galaxies with $I \lesssim 25.5$ (75 sources/arcmin^2).

A merged photometric catalog at all available wavelengths was also constructed for this sample as explained in Pérez-González et al. (2005) and Section 2 2.2. Again, a negligible fraction of the I-band selected sample, only 2%, is detected in less than 5 filters.

More than 90% of the I-band selected sources were also detected in deep $BVRz$ imaging. In these bands, 75% of our I-band sources are brighter than B=26.0, V=25.8, R=25.5, and z=25.1. About 50%-55% of the I-band sample is detected by IRAC (at 3.6 and 4.5 μm; at 5.8 and 8.0 μm, the fraction drops to 40%-45%). MIPS at 24 μm is able to detect about 7% of the I-band sources above $F(24)$=80 μJy.

2.4. *The spectroscopic sample*

Both the HDF-N and the CDF-S include a large compilation of spectroscopic redshifts obtained by several surveys. Unfortunately, there is no public spectroscopic survey in the LHF, so this field could not be used for building templates to estimate photometric redshifts (see Section 3 3.5). In the HDF-N, we used 1,699 spectroscopic redshifts (∼20% of the entire sample in that field) found in Wirth et al. (2004), Cowie et al. (2004), and Reddy et al. (2006a). Only a fraction of those redshifts (1,340 sources) are flagged as high reliability (larger than 80%). In the CDF-S, we compiled 1,410 spectroscopic redshifts (about 15% of the sample in that field), 891 of them flagged as reliable with a probability larger than 80%, from several sources: Le Fèvre et al. (2004), Szokoly et al. (2004), Vanzella et al. (2005), and Vanzella et al. (2006). More than half of the highly-reliable spectroscopic redshifts are below z=1.0 (55% in the CDF-S, and 80% in the HDF-N), and most of them are below z=1.5 (95% in the CDF-S, and 97% in the HDF-N). These spectroscopic redshifts were complemented with photometric redshifts estimated as explained in Section 3 3.5.

2.5. *Star-galaxy separation*

In order to separate galaxies from stars in the merged photometric catalogs, we used 7 criteria, one based on the STELLARITY parameter given by SEXTRACTOR (Bertin & Arnouts 1996), and the other 6 criteria based on color-color and color-magnitude diagrams using optical and NIR fluxes. All objects detected in more than one optical or NIR band, and presenting an average value of the STELLARITY parameter larger than 0.95 were identified as stars. An object was also considered a star if it satisfied any of these color equations (when fluxes were available), extracted from Eisenhardt et al. (2004) and Rowan-Robinson et al. (2005): a) $[3.6]-[8.0] > -2$ and $[3.6]-[8.0] < -1$ and $[8.0] < 20.$, or $[3.6]-[4.5] > -1$ and $[3.6]-[4.5] < -0.5$ and $[4.5] < 19.5$; b) $[5.8]-[8.0] > -1$, $[5.8]-[4.5] < -0.2$ and $[8.0] < 20.$; c) $I-[8.0] < -1$ or $I-[3.6] < 1$ and $[3.6] < 18.$ or $I-[8.0] < -1$ and $[3.6]-[8.0] < -1$; d) $B-I > 2\times(I-[3.6])+0.070$; e) $J-K+0.956 < 0.5$; and f) $[3.6]_{3''}-0.460-[3.6]_{\rm auto} > -0.25$ and $[3.6] < 15.$ and $[3.6]_{3''}-0.460-[3.6]_{\rm auto} < 0.2$, or $[3.6]_{3''}-[3.6]_{\rm auto} < -0.25$, where $[band]_{3''}$ is the magnitude in a 3″ diameter aperture, and $[band]_{\rm auto}$ is the MAG_AUTO magnitude given by SEXTRACTOR (an estimation of the integrated magnitude). The star-galaxy separation for the IRAC sample was checked against the galactic number counts published by Fazio et al. (2004a, see also the stellar number counts predicted by Arendt et al. 1998 and Wainscoat et al. 1992), finding very good agreement with our results (absolute differences of less than 0.1dex at all fluxes down to the limits of our survey). Note that these authors also show that the stars dominate the number counts at the bright end, but they are a minor contributor at faint magnitudes ($[3.6] \gtrsim 18$), the range where our extra-galactic analysis is concentrated.

the determination of the central position of each IRAC source can be determined more accurately (the actual value depending on the brightness of the source) and sources are resolved for separations of the order of ∼1″. This means that if the source positions are known, we can identify and deblend IRAC sources separated ∼1″ from each other (using a similar method to that explained in Grazian et al. 2006).

3. ESTIMATION OF PHOTOMETRIC REDSHIFTS, STELLAR MASSES, AND STAR FORMATION RATES

3.1. *Template generation*

The estimation of the photometric redshift, stellar mass, and SFR of each galaxy in our IRAC and I-band selected samples was carried out in a two step process. Given the significant degeneracies inherent to any stellar population modelling, and in order to get the best estimations of the interesting parameters, we decided to first build a reference set of stellar population and dust emission templates, which could be used afterwards to obtain photometric redshifts, stellar masses, and SFRs for the entire sample. The reference template set was built with the galaxies in our spectroscopic sample with highly reliable redshifts and well-covered (with enough data points from the rest-frame UV to NIR/MIR wavelengths) spectral energy distributions (SEDs). This is the same approach we chose in Pérez-González et al. (2005).

As a major improvement of our photometric redshift technique described in Pérez-González et al. (2005), we (significantly) increased the spectral resolution of the templates by fitting the SEDs of the galaxies in the reference spectroscopic sample with models of the stellar population and dust emission.

3.2. *Stellar population synthesis models*

For the stellar population synthesis, we carried out two sets of fits: 1) one set assuming that the star formation history of each galaxy can be described by a declining exponential law with time scale τ, age t (i.e., $SFR(t) \propto e^{-t/\tau}$), metallicity Z, and attenuated by an amount described by the quantity $A(V)$ (1-POP models, hereafter, see also Gil de Paz & Madore 2002); and 2) another set (2-POP models, hereafter) assuming one recent instantaneous burst of star formation of age $t_{\rm you}$, metallicity $Z_{\rm you}$ and extinction $A(V)_{\rm you}$, overimposed on an evolved stellar population characterized by $\tau_{\rm old}$, $t_{\rm old}$, $Z_{\rm old}$, and $A(V)_{\rm old}$. The attenuation at any wavelength was calculated from the free parameter $A(V)$ using the Charlot & Fall (2000, CF00 hereafter) recipe. In this work, the attenuation of the gas and stellar emissions is divided into three components, based on a simple scenario: the light arising from the newly-formed stars, embedded in a birth cloud, is attenuated by the material in the HII region, by a surrounding shell of molecular and/or non-ionized atomic gas and dust, and finally by the inter-stellar medium. The extinction law is approximated by a power-law function of the form $A_\lambda \propto \lambda^n$ (the authors suggest $n = -0.7$). There is also a dependence of the birth cloud extinction on the age of the stars: for stars younger than 10 Myr (the typical lifetime of molecular clouds) the extinction is μ times larger than for older stars, where $\mu\sim0.3$ (with significant scatter). We also ran a set of models assuming that the attenuation law was similar to the one found for local starbursts by Calzetti et al. (2000, CALZ00 recipe, hereafter). The stellar emission in our models was taken from the PEGASE code (Fioc & Rocca-Volmerange 1997), assuming a Salpeter (1955) initial mass function (IMF) with $0.1<\mathcal{M}<100\ \mathcal{M}_\odot$ and a single power-law slope through the entire mass range. We also added the emission from the gas heated by the stars (emission lines and nebular continuum) using the emission and recombination coefficients given by Ferland (1980) for an electron temperature $T_e = 10^4\,K$, the relations given by Brocklehurst (1971), and the theoretical line-ratios expected for a low density gas ($n_{\rm e} = 10^2\,cm^{-3}$) with $T_{\rm e} = 10^4$ K in the recombination Case B (Osterbrock 1989).

The 1-POP models required 4 parameters to fit. Our fitting routine probed the solution space in the following ranges for the parameters $[\tau, t, Z, A(V)]$: *i*) we assumed τ values from an almost instantaneous burst ($\tau = 1$ Myr) to an almost constant SFR ($\tau = 100$ Gyr) using a logarithmic interval of 0.1dex (in yr) for a total of 51 steps; *ii*) ages were probed from $t = 1$ Myr to $t = 13.5$ Gyr in logarithmic intervals for a total of 60 steps, constraining the solution for each object so the computed age was not larger than the age of the Universe at the redshift of the galaxy; *iii*) we used the 7 discrete values of the metallicity available in the PEGASE code $[0.005, 0.0.02, 0.2, 0.4, 1.0, 2.5, 5.0] \times Z_\odot$; and *iv*) extinction values ranged from $A(V) = 0$ mag to $A(V) = 5$ mag in intervals of 0.10 mag (51 steps).

For the 2-POP models, each one of the 2 stellar populations requires in principle 4 parameters to fit, but we forced the recent burst to be instantaneous, so the young stellar population only requires 3 free parameters to fit. Added to those 7 parameters, one more parameter is necessary, the burst strength b, to describe the fraction of the total stellar mass of the galaxy that the recent burst has created. Our fitting routine probed the solution space in the following ranges for the parameters $[\tau_{\rm old}, t_{\rm old}, Z_{\rm old}, A(V)_{\rm old}, \tau_{\rm you}, t_{\rm you}, Z_{\rm you}, A(V)_{\rm you}, b]$: *i*) $\tau_{\rm old} = 1$ Myr to $\tau_{\rm old} = 100$ Gyr using a logarithmic interval of 0.1dex; *ii*) $t_{\rm old} = 1$ Gyr to $t_{\rm old} = 13.5$ Gyr in logarithmic intervals (constrained by the age of the Universe at the redshift of each galaxy); *iii*) $Z_{\rm old}$= $[0.005, 0.0.02, 0.2, 0.4, 1.0, 2.5, 5.0] \times Z_\odot$; *iv*) $A(V)_{\rm old}$ = 0 mag to $A(V)_{\rm old}$ = 5 mag in intervals of 0.1 mag; *v*) we assumed an instantaneous burst for the recent star formation event (i.e., $\tau_{\rm you}$ = 1 Myr, so actually this is not a free parameter); *vi*) $t_{\rm you}$ = 1 Myr to $t_{\rm you}$ = 1 Gyr in logarithmic intervals (constrained by the age of the Universe at the redshift of each galaxy); *vii*) $Z_{\rm you}$= $[0.005, 0.0.02, 0.2, 0.4, 1.0, 2.5, 5.0] \times Z_\odot$; *viii*) $A(V)_{\rm old}$ = 0 mag to $A(V)_{\rm old}$ = 8 mag in intervals of 0.1 mag; and *ix*) the burst strength could take values from 0.5% to 15% in steps of 0.5%.

3.3. *Stellar population synthesis fitting procedure*

The stellar population synthesis models were compared with the observed photometric data of the galaxies in the spectroscopic sample using a maximum likelihood estimator similar to the one defined in Equation 6 by Pérez-González et al. (2003b), which takes into account the uncertainties in each data point. All data points for rest-frame wavelengths bluer than 4 μm (where stars should dominate the integrated emission of the galaxy) were included in the fit.

Given the large number of possible solutions (1×10^6 in the 1-POP case and 3×10^{11} for the 2-POP models), the amount of photometric data to fit (up to 48 bands in the case of the sources in the CDF-S, 16 in the HDF-N, and 14 in the LHF), and the number of galaxies in our samples (more than 50,000 adding IRAC and I-band selected galaxies), the time requirements to probe the complete solution space for each galaxy (each one at a

certain redshift) were prohibitively high. Therefore, we had to use a minimization procedure to search for the best solution without evaluating the minimization function at all points in the grid of solutions. The minimization procedure was a two step algorithm. First, we used a genetic algorithm that started with 200 "individuals" (i.e., 200 points in the solution space), whose "genome" was formed by the 4 or 8 free parameters in our minimization problem. The 200 individuals were "coupled" randomly (obtaining 100 couples). Each one of these couples (formed by "parents") produced 2 "descendants". Each descendant was built by combining randomly the parameters of the parents and checking that the descendant was a better solution for the minimization problem than its parents. If that was not possible after 10 "births", the best individuals were kept. After every 10 combinations of parameters, we allowed a random mutation in one of them. After all the couples had produced 2 descendants, we eliminated the parents or descendants that produced the worst results for the minimization problem until 200 individuals survived, and then started again the procedure for another generation with the best 200 individuals. The total number of generations was set to 100. For the final generation, we took the 4 best individuals (the best 4 solutions of the minimization problem) and produced small grids of solutions around them (with a width equal to one tenth of the full size of the solution space for each free parameter). We evaluated all the solutions in these grids, and found the best solution and confidence intervals. Our minimization procedure was tested for a subsample of 1,000 galaxies in the 1-POP case by comparing the best solution found by the algorithm with that obtained by evaluating all the grid points in the entire solution space. For this test sample, the minimization algorithm recovered the best solution for $\sim$50% of the galaxies. For the rest of sources, the difference between the best value and the value recovered by the minimization algorithm was always smaller or equal to one tenth of the size of the grid for each free parameter. We will come back to the discussion of the goodness of the minimization algorithm in Section 3 3.6, when we discuss the quality of the derived photometric redshifts, stellar masses, and SFRs.

3.4. *Dust emission models*

Once the stellar spectrum was modeled, we subtracted the predicted fluxes from the photometric data points at rest-frame wavelengths redder than 4 μm (if present) to obtain the emission arising from the dust. This "IR excess" was then fitted with one of the dust emission models of Chary & Elbaz (2001). We selected the model best reproducing the colors of the dust emission, if several photometric points were available (for relatively low redshift; see the second SED fitting example in Figure 1), or the model giving the closest value to the observed monochromatic luminosity if only one IR photometric point was available (see the third example in Figure 1). To check the uncertainties in the derived IR-based SFRs, we also used the models of Dale & Helou (2002) and Rieke et al. (2007, in preparation) in the fitting of the "IR excess".

3.5. *Photometric redshifts, stellar masses, and SFRs*

Our final reference template set is composed of 2,074 galaxies (1,310 galaxies from the HDF-N and 764 from the CDF-S), for which we obtained 1,666 different 1-POP+dust models (each one of them with a unique combination of the free parameters), and 1,958 2-POP+dust models. As mentioned earlier, these galaxies were selected from the spectroscopic sample, all of them having a spectroscopic redshift measured with a reliability probability larger than 80%. In addition, all the reference sources should have more than 10 different photometric data points in their SEDs covering the UV, optical, and NIR/MIR spectral ranges. Three examples of these templates are shown in Figure 1, and discussed in Section 3 3.6. The entire template set is available upon request to the authors.

The photometric redshift estimation for each galaxy in our survey was carried out in a similar way to that described in Pérez-González et al. (2005). Briefly, the observed data (fluxes and uncertainties) were compared with the redshifted models (with steps of Δz=0.01) using a χ^2 minimization algorithm. The technique also includes a preliminary detection of the 1.6 μm bump feature (if present) which helped to constrain the final solution and get rid of outliers. The template giving the best solution at each redshift also had to provide an age of the stellar population younger than the age of the Universe at that redshift. The photometric redshift probability distribution was built with the best values of the χ^2 estimator (corresponding to the model best reproducing the observed SED) at each redshift, and the most probable redshift and uncertainty were estimated from that probability distribution (as a mean weighted with the probabilities, see Bolzonella et al. 2000).

From the best model and most probable photometric redshift, we could also obtain an estimation of the stellar mass, as the model established the monochromatic luminosity per unit of stellar mass at all wavelengths. By scaling this model to the observed monochromatic luminosities (multiplying by a factor), we obtained the stellar mass of each galaxy. The final stellar mass and associated uncertainty for each galaxy were obtained as the average and standard deviation of the stellar masses obtained for each observed photometric band. The uncertainty includes both the effect of the photometric errors and the uncertainty in the determination of the redshift. The average stellar mass uncertainty is 0.2dex, typical of any stellar population study (the typical accuracy of stellar masses obtained with stellar population synthesis models is a factor of 2–3; see, e.g., Fontana et al. 2006; Kauffmann et al. 2003; Pérez-González et al. 2003c; Papovich et al. 2006).

Star formation rates were estimated from the total IR luminosity $[L(8-1000)]$ calculated by integrating the dust emission models for each galaxy between 8 μm and 1000 μm. Galaxies not detected by MIPS at 24 μm were assumed to have an upper limit flux of $F(24) = 60$ μJy. The final SFR estimation also includes the contribution from unobscured star formation detected directly in the UV. According to Bell et al. (2005), we can estimate the total SFR for each galaxy from $L(8-1000)$ and $L(0.28)$, where $L(0.28) = \nu L_\nu(0.28)$ is the monochromatic luminosity at 0.28 μm measured directly from the stellar population model for each galaxy. The conversion factor is taken from Kennicutt (1998) for a Salpeter (1955) IMF:

$$SFR = 1.8\times10^{-10}[L(8-1000)+3.3L(0.28)]/L_{\odot}\ \mathcal{M}_{\odot}\mathrm{yr}^{-1} \quad (1)$$

In order to characterize the uncertainties of the SFRs derived with our models, we also calculated IR-based SFRs by estimating monochromatic luminosities at rest-frame wavelengths 6.7 μm, 12 μm, and 15 μm. The integrated luminosity $L(8-1000)$ can be obtained from these monochromatic luminosities by applying the empirical relationships found in Chary & Elbaz (2001). Another estimation of the SFR can be obtained from the rest-frame monochromatic luminosity at 24 μm applying the equation given in Alonso-Herrero et al. (2006). We will discuss the uncertainties in the SFR estimations in Section 3 3.6 3.6.4.

3.6. *Evaluation of the modelling procedure and derived parameters*

3.6.1. *Some examples of SED fits*

Figure 1 shows three examples of the dust and stellar population models for IRAC sources at different redshifts. The three panels on the left show the fits for the 1-POP case, and the three panels on the right show the fits for the 2-POP case for the same sources.

The upper two panels present a source nicely fitted by a single old stellar population with intermediate extinction, no current star formation (a bulge dominated galaxy), and no detection at 24 μm. In this case, although the photometry at rest-frame wavelengths redder than 4 μm was not used in the model fitting, those points are well reproduced with just stellar emission. When fitting the same SED with a 2-POP model, we recover very similar parameters to the 1-POP case, with a minor contribution (just 1% in mass) from a more recent burst. Note that both types of models give very similar stellar mass values.

The second example (middle row) shows an intermediate redshift galaxy detected at 24 μm. This galaxy can be fitted either by an old single stellar population with a large extinction or with a combination of an old stellar population with very low attenuation and a more recent burst contributing about 13% to the total stellar mass of the galaxy. This recent burst presents a relatively large dust attenuation that could be responsible for the emission in the MIR/FIR (the galaxy is detected at 24 μm). For this galaxy, dust emits a significant fraction (about 50%) of the 8 μm luminosity (rest-frame 4 μm) and almost 100% of the 24 μm luminosity (rest-frame 12 μm). The 1-POP models give a larger stellar mass value than the 2-POP models (still, the difference is a factor of 3, comparable to the typical uncertainty in stellar population studies) because a lot of stars are necessary to fit the high NIR photometric data points, while a lot of extinction is necessary to simultaneously fit the UV/optical fluxes.

The third example (bottom row) is a high redshift galaxy with a very blue spectrum. It can be fitted either with an almost continuous unattenuated star formation (based on the high τ value) lasting about 100 Myr, or with a similar primary burst (producing 93% of all the stellar mass) followed by a more recent (10 Myr) and much more attenuated ($A(V)_{\rm you}$=7 mag and a strong MIR emission detected at 24 μm) event of star formation. Note also that the IRAC photometric point at 8.0 μm is too high in comparison with the combined star+dust models. At wavelengths around $\lambda\sim$4–10 μm or even at $\lambda\sim$2–10 μm for very luminous IR sources, the integrated emission comes from both the dust and the stars in comparable fractions. In this overlap region between the dust and stellar models, the spectrum may show prominent emission-lines or PAH features which are not found in the stellar and dust emission models. For example, there is a PAH feature at rest-frame 3.3 μm (very weak in all dust models in the Chary & Elbaz 2001 or Dale & Helou 2002 libraries) which may have a non-negligible contribution to the global emission in this spectral region.

3.6.2. *Statistical evaluation of the photometric redshifts*

The main three parameters that we want to extract from the SED fits are the photometric redshift, the stellar mass, and the SFR of each galaxy. The quality of our photometric redshifts is checked in Figure 2 for the fields with extensive spectroscopic data: the HDF-N and the CDF-S. Unfortunately, given that there is not a systematic public spectroscopic survey in the LHF, we cannot check our photometric redshifts directly in this field. In spite of this, the photometry in the LHF is as good or even better (given that the optical images are ultra-deep observations taken with Subaru) than in the other two fields, and the general redshift distribution for the LHF sources is similar to that in the HDF-N and the CDF-S. Consequently, we conclude that the quality of the photometric redshifts in the LHF must be comparable to the other two fields (see also the discussion about the redshift distribution of our sample in Section 4).

The top panel of Figure 2 shows the comparison of our photometric redshifts and spectroscopic redshifts for the IRAC selected sample in the HDF-N (for the 1,699 sources with available spectroscopy). The average (median) redshift difference ($\delta z = z_{\rm spec} - z_{\rm photo}$) is 0.014 (0.010), comparable to the redshift step used in our photometric redshift technique. This demonstrates that there are no systematic errors in our redshifts. Almost all sources, 95%, have values of $\sigma_z/(1+z)<0.2$ (where σ_z is the absolute value of δz), 88% of the objects present values of $\sigma_z/(1+z)<0.1$, and 70% have $\sigma_z/(1+z)<0.05$. The average (median) value of $\sigma_z/(1+z)$ is 0.055 (0.032). Very similar statistics are obtained for the I-band selected sample: 94% of these sources present $\sigma_z/(1+z)<0.2$, 86% $\sigma_z/(1+z)<0.1$, and the average (median) $\sigma_z/(1+z)$ is 0.060 (0.036).

The quality of the photometric redshifts in the CDF-S for IRAC selected sources is shown in the bottom panel of Figure 2. The average (median) value δz is 0.020 (0.015). In this field, 93% of the objects have values of $\sigma_z/(1+z)<0.2$, 85% of the objects have values of $\sigma_z/(1+z)<0.1$, and 67% have $\sigma_z/(1+z)<0.05$. The average (median) $\sigma_z/(1+z)$ is 0.060 (0.040). For the I-band selected sources, the numbers are similar: 92% of these sources present $\sigma_z/(1+z)<0.2$, 80% $\sigma_z/(1+z)<0.1$, and the average (median) $\sigma_z/(1+z)$ is 0.080 (0.047).

The photometric redshift error distribution for different magnitude and redshift intervals are used in Section 5 to estimate the uncertainties in the stellar mass functions. In addition, the redshift intervals in that Section and the following are constructed assuming that the typi-

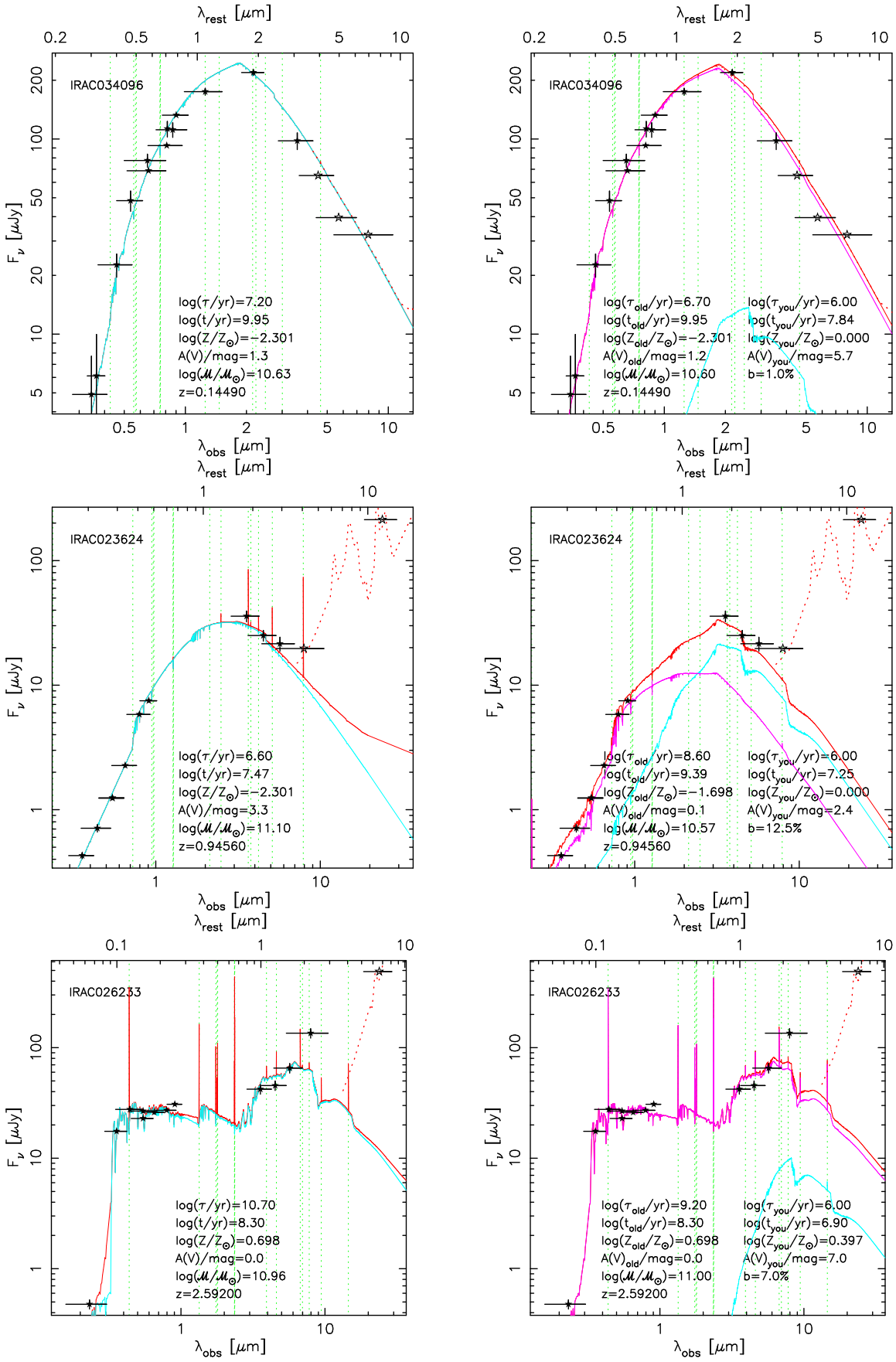

FIG. 1.— Three examples of the stellar population and dust emission modelling of IRAC selected sources in the spectroscopic sample. The spectroscopic redshift and main stellar population parameters of the best fit are given in each panel. Filled black stars and vertical error bars show the photometric points used in the stellar population fits (wavelengths bluer than 4 μm). Horizontal error bars for each photometric point show the width of the filter. Open black stars are the photometric data points used in the modelling of the dust emission. The left panel of each row shows the 1-POP stellar emission fits with a cyan line, and the final fit (including nebular continuum and emission lines) with a red continuous line. On the right panel of each row, the same SEDs have been fitted with the 2-POP models, where one stellar population is plotted with a cyan line, the other population with a magenta line, and the addition of both with a red line (including nebular continuum and emission lines). For all panels, the dust emission model taken from Chary & Elbaz (2001) which best reproduces the MIR emission (if present) has been plotted with a dashed red line. Green vertical lines show the positions of the most interesting emission-lines in the optical and NIR spectral ranges.

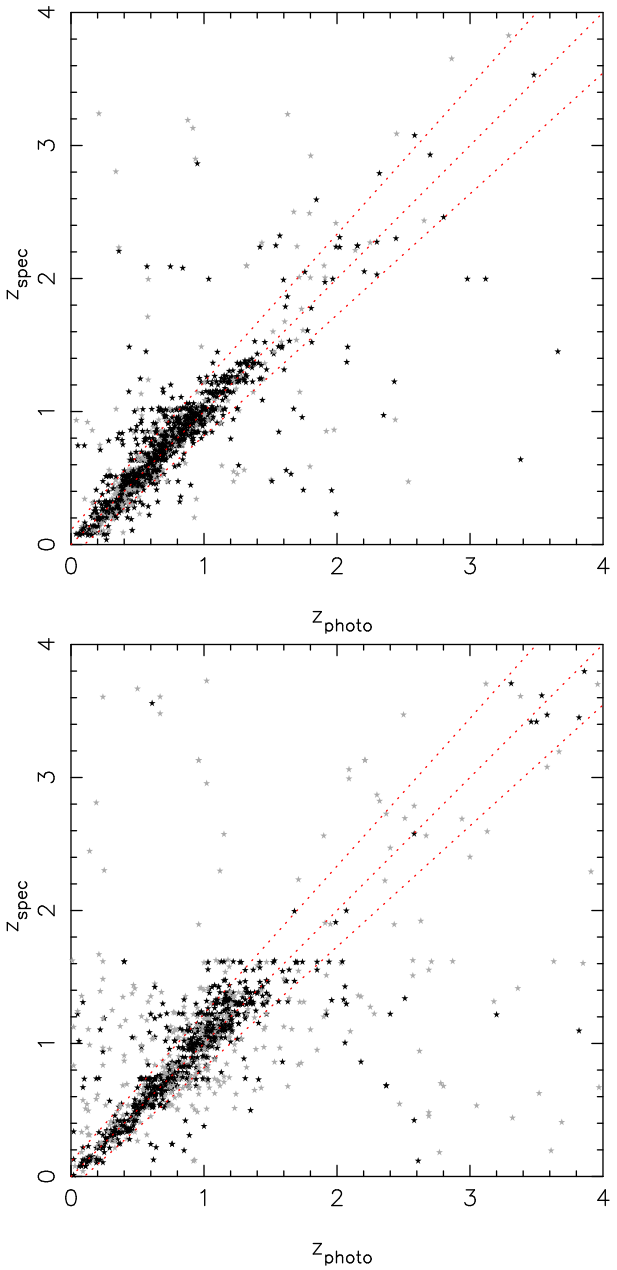

FIG. 2.— Comparison of the spectroscopic and photometric redshifts for IRAC selected sources in the HDF-N (top panel) and the CDF-S (bottom panel). Gray symbols are sources with spectroscopic redshifts which have a reliability probability lower than 80%. Open stars are sources detected in less than five bands. The dashed lines show the equality line, and the $\sigma_z/(1+z)<0.1$ area.

cal photometric redshift error is $\sigma_z/(1+z)\sim0.1$ (equation valid for more than 85% of our sample).

3.6.3. *Statistical evaluation of the stellar masses*

In this section, we discuss the quality of our stellar masses, and the possible systematics introduced by our fitting algorithm and the *a priori* assumptions of the models.

First, we checked how well the minimization algorithm of our SED fitting technique recovered the stellar mass value corresponding to the model best fitting the data. For that purpose, we used 1,000 randomly selected galaxies for which we probed all the nodes in the solution grid for the 1-POP case (for the 2-POP case, the number of points in the solution grid is too large to attempt the individual evaluation of all of them). On average, the difference between the stellar mass estimated with the minimization algorithm and the stellar mass given by the model best fitting the SED is 0.002dex, the median is 0.000dex, the standard deviation is 0.07dex, and there are not any absolute differences larger than 0.30dex. These statistics confirm that the minimization algorithm is able to recover the best stellar mass estimate within the typical uncertainties in stellar populations synthesis analysis (a factor of 2–3).

We also compared the stellar masses obtained with the 1-POP and 2-POP models. For about 70% (55%) of the galaxies, both estimates are equal within a factor of 0.3dex (0.2dex). However, for the rest of galaxies (most of them with $\mathcal{M}<10^{10.5}$ $\mathcal{M}_\odot$), the 2-POP estimates are higher (with the most extreme cases showing a difference of up to a factor of 10). On average, stellar masses derived with 2-POP models are 0.18dex higher than those derived with 1-POP models. This can be explained by the fact that most of the photometric data points in the modelling fits are found in UV/optical wavelengths, where the emission of relatively young stars is significant. Older stars, possibly much more numerous and dominating the global stellar mass of a galaxy, may be hidden by the intensity of more recent starbursts. This effect should be more noticeable in less massive systems presenting bright recent bursts involving a relatively high fraction of the total stellar mass of the galaxy. Only in the 2-POP models are we able to take this effect into account, and that is why in this case we systematically obtain larger stellar masses for some galaxies. We conclude that the choice of the 1-POP or 2-POP models does not change the stellar masses significantly (more than the typical uncertainties of a factor of 2–3) in a statistical sense.

The stellar masses obtained with the PEGASE code (Fioc & Rocca-Volmerange 1997) were compared with the values estimated by using the BC03 models from Bruzual & Charlot (2003). On average, the BC03 models give stellar masses larger by 0.03dex (less than 10%), with a scatter of 0.18dex. For 95% of the galaxies, the stellar mass difference is lower than a factor of 3. We also fitted the SEDs with the M05 models developed by Maraston (2005, see also Bruzual 2007), which include a more refined treatment of the emission from thermally pulsating asymptotic giant branch stars, and are claimed to obtain stellar masses that can be lower by as much as 60% (based on the prediction of lower NIR mass-to-light ratios for some ages). On average, the M05 models give stellar masses smaller by 0.14dex (less than 30%), with a scatter of 0.22dex. For 96% of the galaxies, the stellar mass difference is lower than a factor of 3.

One important *a priori* assumption of any stellar population modelling is the treatment of extinction by dust. We compared the stellar masses obtained with the two different extinction recipes we considered (CF00 and CALZ00). For about 80% (65%) of the galaxies, both estimates are equal within a factor of 0.3dex (0.2dex). For the rest of galaxies (again, most of them with $\mathcal{M}<10^{10.5}$ $\mathcal{M}_\odot$), the estimates using the CF00 recipe

are higher up to a factor of 5. On average, stellar masses derived with the CF00 recipe are 0.10dex higher than those derived with CALZ00 law. As discussed in Pérez-González et al. (2003c), in the CF00 recipe the attenuation of the emission arising from the stars is always (except for very young bursts) larger than the attenuation of the gas emission. The CALZ00 recipe shows a opposite behavior, given that the attenuation of the stellar emission is roughly half of the attenuation of the gas emission. Moreover, the attenuation wavelength dependence (from the UV to the NIR) proposed by CF00 is shallower than the one in CALZ00. This leads to a need of more stars to obtain the same observed luminosity for equal values of the extinction in the CF00 case, which explains the larger stellar masses derived for this case (on average). However, the final effect on the masses is of the order of 0.1dex, which demonstrates that choice of an extinction recipe does not change the stellar masses more than the typical uncertainties.

Another important assumption of the stellar population models is the IMF, which has a direct effect on the derived stellar masses. Different IMFs produce stellar spectra with very similar colors, but with less or more stars, which causes a systematic uncertainty in the final stellar mass estimations. For example, a Kroupa et al. (1993) IMF (as the one used in Borch et al. 2006) predicts stellar masses smaller than ours by a factor of $\sim$1.7, or a Baldry & Glazebrook (2003) IMF (used in, for example, Glazebrook et al. 2004) predicts also smaller masses by a factor of $\sim$1.8. All our results and those extracted from the literature were normalized to a Salpeter (1955) IMF with $0.1<\mathcal{M}<100\,\mathcal{M}_{\odot}$. If the IMF is universal (the same at all redshifts), this choice should not affect our results other than an overall normalization. A discussion about changes in the IMF from galaxy to galaxy is far out of scope of this paper.

Finally, we performed another test of the goodness of our stellar mass estimates by comparing the results obtained from direct comparison of the SEDs with the entire grid of stellar population models (once the redshift of a galaxy is known) with the results obtained with the photometric redshift technique using the empirically built set of models, from which we obtained stellar mass estimates for all galaxies. We find a very good agreement between these two stellar mass calculations: 90% of galaxies present an average difference between the two mass estimates of less than 0.01dex, and the scatter around this value is 0.15dex.

Based on this discussion, the choices of 1-POP or 2-POP models, distinct stellar population libraries, different IMFs, or different extinction recipes produce changes in the derived stellar masses of the same order or smaller than the typical error in any stellar population synthesis analysis (a factor of 2–3), directly linked to the degeneracies of the solutions to the problem. Thus, in the following Sections we will only present our results obtained with the stellar masses estimated with the 1-POP models, the Calzetti et al. (2000) extinction law, and a Salpeter (1955) IMF. This choice will also allow us to compare directly with other previous works found in the literature, that usually assume these characteristics in their modelling procedures.

3.6.4. *Statistical evaluation of the SFRs*

In order to understand the systematic and random uncertainties of our estimations of the SFR for each galaxy, we carried out two tests.

First, we used 3 different dust emission template sets built by Chary & Elbaz (2001), Dale & Helou (2002), and Rieke et al. (2007, in preparation). The values of the IR SFR [estimated from $L(8-1000)$ using the conversion factor found in Kennicutt 1998] derived with the Chary & Elbaz (2001) models were systematically smaller than the SFRs derived with the Dale & Helou (2002) models (on average, 0.1dex) and Rieke et al. (2007, in preparation) templates (on average, 0.2dex). To take into account the systematic uncertainties introduced by the use of a particular set of models, we finally considered an average value of the estimations from the three template sets. The typical uncertainty of this average value (based on the standard deviation of the 3 estimations) is about 50%.

The second test consisted in obtaining IR-based SFRs with different methods. Classically, IR-based SFRs are calculated from the integrated IR luminosity $L(8-1000)$. The quantity $L(8-1000)$ can be estimated for each galaxy by fitting the IR spectrum with models of the dust emission. For our galaxies, this translates to a significant extrapolation in the templates, since the reddest point in our SEDs corresponds to the observed MIPS 24 μm emission, and we are assuming that a color or a single photometric point in the MIR is closely related to the emission in the FIR, which dominates the integrated IR luminosity. However, one can also avoid this large extrapolation by estimating monochromatic luminosities at specific wavelengths which are not far from the reddest photometric point in our SEDs. In this sense, we estimated monochromatic luminosities at 6.7 μm, 12 μm, and 15 μm, and then calculated the integrated luminosities $L(8-1000)$ using the empirical relationships built by Chary & Elbaz (2001). Another independent SFR estimation was obtained by interpolating in the models to measure the rest-frame MIPS 24 μm monochromatic luminosity. This luminosity was converted to a SFR using the calibration given in Alonso-Herrero et al. (2006). The typical scatter of these different IR-based SFR estimations obtained from monochromatic emissions is 30%.

From these tests, we conclude that our IR-based SFR estimations are good within a factor of 2, which is consistent with other evaluations of IR-based SFRs (e.g., Caputi et al. 2006; Le Floc'h et al. 2005; Papovich & Bell 2002).

4. REDSHIFT DISTRIBUTION OF OUR SAMPLE

Figure 3 shows the redshift distribution of our IRAC selected sample (average number density and number densities in each field), and the subsample detected also by MIPS at 24 μm. Only sources with fluxes above our 75% completeness levels are included. The distributions have been constructed taking into account the typical photometric redshift error ($\sigma_z/(1+z)\sim0.1$), i.e, Figure 3 represents the real redshift distribution convolved with the photometric redshift probability distribution.

Figure 3 demonstrates the importance of cosmic variance effects on deep photometric surveys. Indeed, large scale structures are clearly visible and located at different redshifts for our 3 fields, especially at $z\lesssim1$. The HDF-N shows two very prominent density peaks at $z\sim0.5$

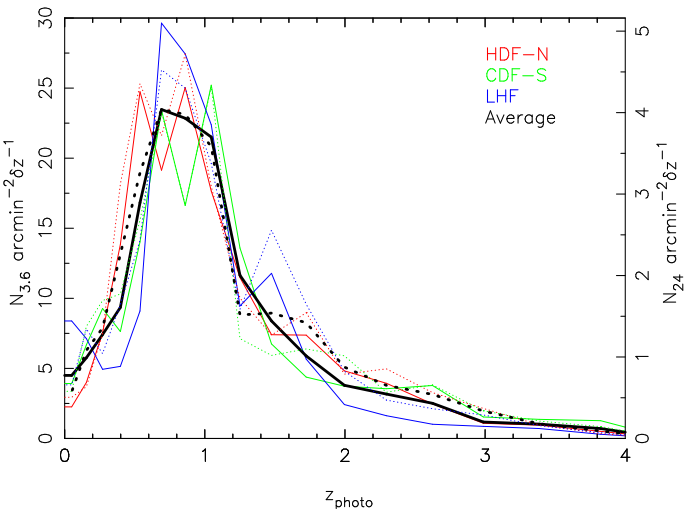

FIG. 3.— Redshift distribution of our IRAC selected sample (including all galaxies above the 75% completeness level). The three fields used in this paper are plotted with different colors, and the average number densities are plotted in black. Continuous lines refer to the number densities for the entire IRAC selected sample (scale on the left vertical axis), and dashed lines refer to the subsample detected also at 24 μm (scale on the right vertical axis). A similar redshift distribution is obtained for the I-band selected sample.

and z∼0.9, consistent with the spectroscopic redshift histogram found in figure 16 of Wirth et al. (2004). There are also minor prominences at z=1.5–2.0 and z=2.0–2.5, which are also seen in the spectroscopic follow-up of UV-selected galaxies in Reddy et al. (2006a). The CDF-S presents very prominent density peaks at z∼ 0.3, z∼0.7, and a broad bump between z∼1.1 and z∼1.4, which coincides (after convolution with the typical photometric redshift uncertainty) with the most prominent spectroscopically confirmed peaks found in figure 7 of Vanzella et al. (2006). The LHF shows an enhanced density at z$\lesssim$0.3, z∼0.7-1.0 and a very prominent peak at z=1.5–1.8, consistent with the high density of x-ray sources found by Mainieri et al. (2002) and Zappacosta et al. (2005) at z∼0.8 and z∼1.6–1.8, and the analysis of the shallower IRAC SWIRE data in Rowan-Robinson et al. (2005).

Only by combining data for several fields are we able to smooth out cosmic variance effects. Indeed, the average redshift distributions for IRAC sources (black continuous line) and MIPS sources (black dashed line) are much smoother than the analogous curves for the individual fields. The shape of the redshift distribution for the IRAC sample is typical of a flux limited sample with a roughly homogeneous detection probability, i.e, the detection of a source depends only on its magnitude (see, e.g., Benítez 2000). The detection probability of our IRAC survey peaks at around z=0.8–1.0. For z<0.6, the detection of sources is dominated by the surveyed volume, and after z∼1.0, the detection probability decreases exponentially up to z∼4. About half of our sample lies at z$\gtrsim$0.9, ∼40% at z>1, and ∼20% at z>1.5. The bulk of the galaxies in this study (∼90%) lie at z<2. This implies that our results about stellar mass functions and densities are very robust up to z∼2, just where our photometric redshifts are empirically well tested. Beyond that point, we still include ∼3000 galaxies, enough to still obtain statistically meaningful results (although systematic errors such as redshift outliers will also contribute more to the errors above z=2). The statistics for the I-band selected sample are very similar to those for the IRAC sample: the average distribution peaks at around z=0.7, and then decays exponentially, enclosing about 50% of the sources below z=0.9, 80% at z<1.5, and 10% at z>2.0.

Figure 3 also shows the redshift distribution of the IRAC sources detected by MIPS at 24 μm and having $F(24)$=80 μJy (dashed lines). The redshift distribution is similar to that presented in Pérez-González et al. (2005), but the improvement in the photometric redshift estimations reveals a more pronounced density bump at z∼1.7 and a weak bump at z∼2.6. The origin of these bumps can be found in the increase of the detection probability induced by prominent PAH features entering the MIPS 24 μm filter as we move to higher redshifts (see also Caputi et al. 2006). Indeed, a typical PAH spectrum shows an absence of features around λ=10 μm, which produces the detection local minimum at z∼1.3 observed in Figure 3. At 6$\lesssim\lambda\lesssim$10 μm, there are several PAH features (the most prominent at 5.5 μm and 7.7 μm) that are responsible for the bumps in the redshift distribution. Note that the final detected density for MIPS sources is a convolution of the real redshift distribution of galaxies (affected by large scale structure), the detection probability (dependent on the limiting flux of the survey and the spectra of the galaxies), and the photometric redshift uncertainty distribution. These two effects (detection probability and photometric redshift uncertainties) result in blurring out redshift-dependent features so they are at lower contrast to the overall real distribution.

5. STELLAR MASS FUNCTIONS AND DENSITIES

5.1. *Completeness of the sample*

Figure 4 shows the distribution of stellar masses of individual galaxies in our IRAC survey as a function of redshift. The blue line shows the stellar mass corresponding to a passively evolving galaxy formed in a single instantaneous burst of star formation occurred at z=∞ and having a 3.6 μm flux equal to the 75% completeness level of our IRAC sample. The stellar mass calculated in this way assumes the maximum mass-to-light ratio, that given by the oldest instantaneously formed stellar population possible at each redshift. Any burst occurring after the primary placed at z=∞ should decrease the observed mass-to-light ratio, thus giving a smaller stellar mass. Therefore, the values given by the blue curve in Figure 4 are the minimum stellar masses that a maximally old galaxy with a flux equal to the 3.6 μm 75% completeness level should present, and we must be detecting all galaxies (actually, at least 75% of all galaxies) with stellar masses above this curve present in the surveyed volume. Note that if the density of galaxies of a given stellar mass at a certain redshift is very small, our surveyed volume may not be large enough to enclose any galaxy of that mass (we would not detect any, although there certainly exist galaxies of that mass in the Universe at that redshift). This is the effect seen in Figure 4 at

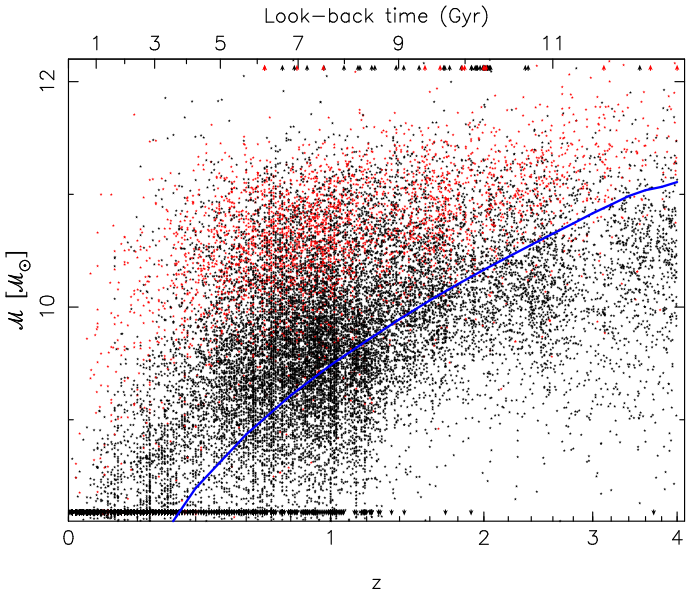

FIG. 4.— Distribution of the stellar masses of all individual galaxies in the IRAC (all symbols) and MIPS (red symbols) selected samples as a function of redshift (shown with a logarithmic scale in the quantity 1+z in the bottom horizontal axis and the corresponding look-back times in the top axis). The blue line shows the stellar mass value at each redshift above which our IRAC survey is 75% complete. Sources whose stellar mass is beyond the vertical axis scale are plotted with arrows at the source redshift.

high stellar masses: at z<0.2, our surveyed volume is not enough to detect galaxies with $\mathcal{M}\gtrsim10^{11.0}$ $\mathcal{M}_\odot$, and we can only detect galaxies with $\mathcal{M}\gtrsim10^{12.0}$ $\mathcal{M}_\odot$ at z$\gtrsim$0.8.

The estimations of the stellar mass functions in the following sections will be carried out for stellar masses above the completeness level shown in Figure 4, i.e., no completeness correction will be carried out to try to recover the stellar mass function at smaller masses (below the blue curve in Figure 4).

5.2. *Stellar mass function estimation procedure*

The entire redshift range 0<z<4 was divided into 12 intervals, the size of each bin chosen to have a statistically representative number of galaxies and taking into account the typical photometric redshift errors. For each redshift bin, we estimated a bivariate luminosity-stellar mass function. The procedure is identical to that used in Pérez-González et al. (2003a). The bivariate luminosity-stellar mass function, BLMF or $\Phi(L,\mathcal{M})$, is defined as the number density of galaxies (in a limited co-moving volume given by our surveyed area and the redshift interval considered) with a given luminosity in a certain band and a given stellar mass. This definition is an extension of the bivariate luminosity function (Loveday 2000). The estimation of the BLMF was performed with a stepwise maximum likelihood (SWML) technique (Efstathiou et al. 1988, see also Willmer 1997), extended to consider two independent variables. In the classical SWML method, the errors in the BLMF are estimated from the covariance matrix. In our case, the estimation of the BLMF uncertainties was carried out by combining the SWML technique with a Montecarlo method to take into account the photometric redshift errors and outliers, as we did in Pérez-González et al. (2005, see also Chen et al. 2003).

To estimate stellar mass functions, we used the IRAC 3.6 μm band as the luminosity variable in the BLMF, given that this is the filter where the selection of the sample was carried out. For the I-band selected sample, we used the I filter as the selection band. Once the BLMF is estimated, if we integrate it through all luminosities, we can estimate the number density of galaxies with a given stellar mass, i.e., the stellar mass function, SMF or $\phi_{\rm SM}(\mathcal{M})$. We only estimated the stellar mass function down to the completeness threshold of the stellar mass discussed in Section 5 5.1.

The results for the SMF were fitted with a smooth function using a Schechter (1976) parametrization, to facilitate comparison with similar fits in the literature. For the 4 bins at highest redshifts, the faint-end slope of the SMF was poorly constrained by our data, so we combined our results with other estimations of the stellar mass functions found in the literature. These estimations are based on the analysis of galaxy samples typically selected at optical wavelengths, thus being more effective than us in probing the low mass regime of the stellar mass function. The SMF points, errors, and Schechter fits for each redshift bin are shown in Figures 5 and 6 (black filled and open stars for the IRAC and I-band selected samples, respectively). These figures also show other SMF estimations found in the literature (color points, see captions for references). The plots also depict the SMFs and fits for the subsample of galaxies detected simultaneously by IRAC and MIPS at 24 μm (filled circles). The data points and Schechter fit parameters are given in the electronic Tables 2 and 3, respectively.

5.3. *The local stellar mass function and density*

Figure 5 shows our estimations of the local stellar mass function (including sources at 0.0<z<0.2) based on both the IRAC (filled stars) and I-band (open stars) selected samples. Given that we are surveying a very limited volume in the local Universe, we do not detect many sources with $\mathcal{M}>10^{11.0}$ $\mathcal{M}_\odot$ (this explains the large errors in this mass regime), but our statistics are much better at low masses. Our results are very similar to those published by Cole et al. (2001) and Bell et al. (2003) based on NIR 2MASS data down to the completeness limit of their surveys ($\mathcal{M}\sim10^{9.5}$ $\mathcal{M}_\odot$). Our deeper data confirm the faint-end slope estimated by Cole et al. (2001) down to even smaller masses, $\mathcal{M}\sim10^{9.0}$ $\mathcal{M}_\odot$. We also find a steepening of the stellar mass function at $\mathcal{M}\lesssim10^{9.0}$ $\mathcal{M}_\odot$ (at least for $\mathcal{M}\gtrsim10^{7.9}$ $\mathcal{M}_\odot$, our completeness level at z$\sim$0).

By integrating our local SMF, we obtain a value for the local stellar mass density of $\rho_*=10^{8.74\pm0.11}$ $\mathcal{M}_\odot$ Mpc^{-3}, in excellent agreement with the values found in Salucci & Persic (1999), Cole et al. (2001), and Bell et al. (2003) ($\rho_*=10^{8.75,8.76,8.74}$ $\mathcal{M}_\odot$ Mpc^{-3}, respectively). The steepening of the stellar mass function at $\mathcal{M}\lesssim10^{9.0}$ $\mathcal{M}_\odot$ has no significant effect on the integrated stellar mass density: the galaxies with $10^{7.8}<\mathcal{M}<10^{9.0}$ $\mathcal{M}_\odot$ contribute less than 3% to the total stellar mass density.

Figure 5 also shows the SMF of the sources detected by MIPS at 24 μm, i.e., the galaxies with active star formation (filled circles and dashed line fit). The MIPS results (data points and fit) are in excellent agreement

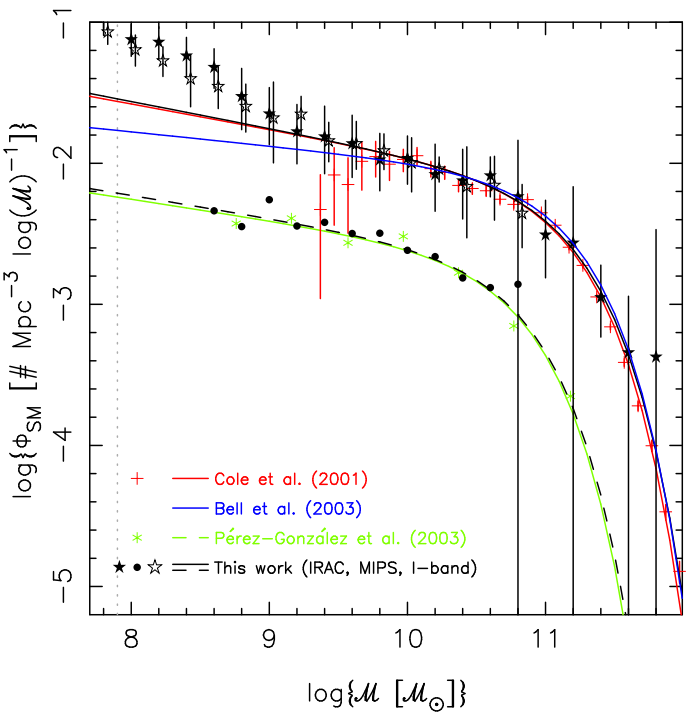

FIG. 5.— Local stellar mass function estimated with the IRAC selected (filled stars), *I*-band selected (open stars), and MIPS selected (filled circles) samples at z<0.2. For clarity, the *I*-band data points have been artificially drifted from the original x-position (the same as the ones for the IRAC selected sample) and we do not show the uncertainties for the MIPS data points. The vertical gray dashed line shows the completeness level of our IRAC survey in the local Universe. The Schechter fit to the IRAC and *I*-band data is shown with a black continuous line. Our estimation of the local stellar mass function is compared with the one estimated by Cole et al. (2001, red crosses and line), and by Bell et al. (2003, blue line). The best Schechter fit to the data for the MIPS sample (i.e., for local star-forming galaxies) is plotted with a dashed line. This SMF is compared with the one published by Pérez-González et al. (2003a, green asterisks and line) for Hα-selected local star-forming galaxies.

with those published by Pérez-González et al. (2003a) for a Hα-selected sample of star-forming galaxies in the local Universe. The local stellar mass density locked in star-forming galaxies is $\rho_*^{SF}=10^{7.84\pm0.08}\ \mathcal{M}_\odot\ \mathrm{Mpc}^{-3}$, i.e., 13±4% of the global stellar mass density in the local Universe is found in active star-forming galaxies. Figure 5 also shows that approximately 1 of every 4 galaxies in the local Universe with $\mathcal{M}\lesssim10^{10.5}\ \mathcal{M}_\odot$ is forming stars currently and would be detected in the IR or with a SFR tracer such as the Hα emission. At higher stellar masses, the fraction of star-forming galaxies decreases by more than a factor of 2 (e.g., ∼10% of all galaxies with $\mathcal{M}=10^{11.0}\ \mathcal{M}_\odot$ are forming stars actively).

5.4. *The evolution of the stellar mass function*

Figure 6 presents the global stellar mass functions estimated in the 12 redshift intervals up to z=4. We show the results obtained with the IRAC selected (filled black stars), the *I*-band selected (open black stars), and the MIPS selected (filled circles) samples. Other estimations found in the literature are also plotted at each redshift interval (normalized to the Salpeter 1955 IMF). We have fitted our SMF data points (and for z>1, also the data points from other works to better constrain the slope at lighter masses) to a Schechter function. In the case of the 24 μm galaxies, we assumed the same faint-end slope estimated for the global SMF.

Our results show that the local density of galaxies (shown with a gray line in all panels) with masses $\mathcal{M}\gtrsim10^{12}\ \mathcal{M}_\odot$ was already reached by the SMF at z=2.5-3.0, i.e., the most massive galaxies were already in place at that redshift (approximately 11 Gyr ago). The mass assembly of galaxies shifts to smaller masses as we move to lower redshifts. By z∼1, the SMF has reached nearly the local density for galaxies with $\mathcal{M}\gtrsim10^{11.8}\ \mathcal{M}_\odot$. At z<1, the star formation in the Universe occurs mainly in galaxies with $\mathcal{M}\lesssim10^{11.5}\ \mathcal{M}_\odot$. It is also interesting to notice the significant evolution (approximately a factor of 0.2dex or 60%, as shown by our data, and also confirmed by the results of Pannella et al. 2006 and Borch et al. 2006) of the SMF between z∼0.4 and z=0 (i.e., a period of 4 Gyr) for stellar masses $10^9\lesssim\mathcal{M}\lesssim10^{11}\ \mathcal{M}_\odot$. We will comment more on this recent evolution in Section 5 5.5.

Figure 6 also shows that the slope of the SMF at low masses remains approximately constant up to at least z∼2 at a value α=-1.2±0.1 (consistent with the models in Nagamine et al. 2005b). Only at very low masses ($\mathcal{M}\lesssim10^{9.0}\ \mathcal{M}_\odot$ at z<1 and $\mathcal{M}\lesssim10^{10.0}\ \mathcal{M}_\odot$ at higher redshifts), the SMF seems to become steeper (based on our results and those from other surveys), but this steepening has a minor effect on the global stellar mass density.

5.5. *The evolution of the cosmic stellar mass density*

The SMFs were integrated for all masses above the completeness level to obtain the observed cosmic comoving stellar mass density. We also integrated the Schechter fits to estimate an extrapolated value of the cosmic stellar mass density at each redshift interval. In Figure 7, we present these results, comparing them with other estimations of the stellar mass density available in the literature (see the captions of Figures 6 and 7 for references). Our central data points are fitted with a Chebyshev polynomial with variable (1+z) and 8$^{\mathrm{th}}$ order [6] (the minimum order necessary to fit the data).

Figure 7 shows that there is a relatively large increase (by a factor of ∼1.3) in the stellar mass density of the Universe in the last 4 Gyr (from z∼0.4 to z=0). This result is confirmed not only by our work, but also by all the stellar mass density estimations at z<0.4 (Salucci & Persic 1999 and Cole et al. 2001 in the local Universe, and Brinchmann & Ellis 2000 and Borch et al. 2006 at $z\lesssim0.4$). As we discussed in Section 5 5.4, this significant recent evolution of the stellar mass density is mainly due to a ∼60% increase in the number density of galaxies with $10^9\lesssim\mathcal{M}\lesssim10^{11}\ \mathcal{M}_\odot$. As suggested by Tresse et al. (2006), since the cosmic SFR density continues to decline or stays at a very low value at z=0−0.4 (based on SFR tracers at all wavelengths; see, e.g., Pérez-González et al. 2005), the number density increase in the last 4 Gyr must have occurred by either accretion of small satellite galaxies or by major mergers between gas-depleted galax-

[6] The coefficients of the Chebyshev polynomial fit (with variable 1+z) to the stellar mass density evolution are $[3.753\times10^8, -2.317\times10^8, 9.126\times10^7, -2.815\times10^7, 1.704\times10^6, -4.331\times10^6, 1.132\times10^7, -1.457\times10^7]$.

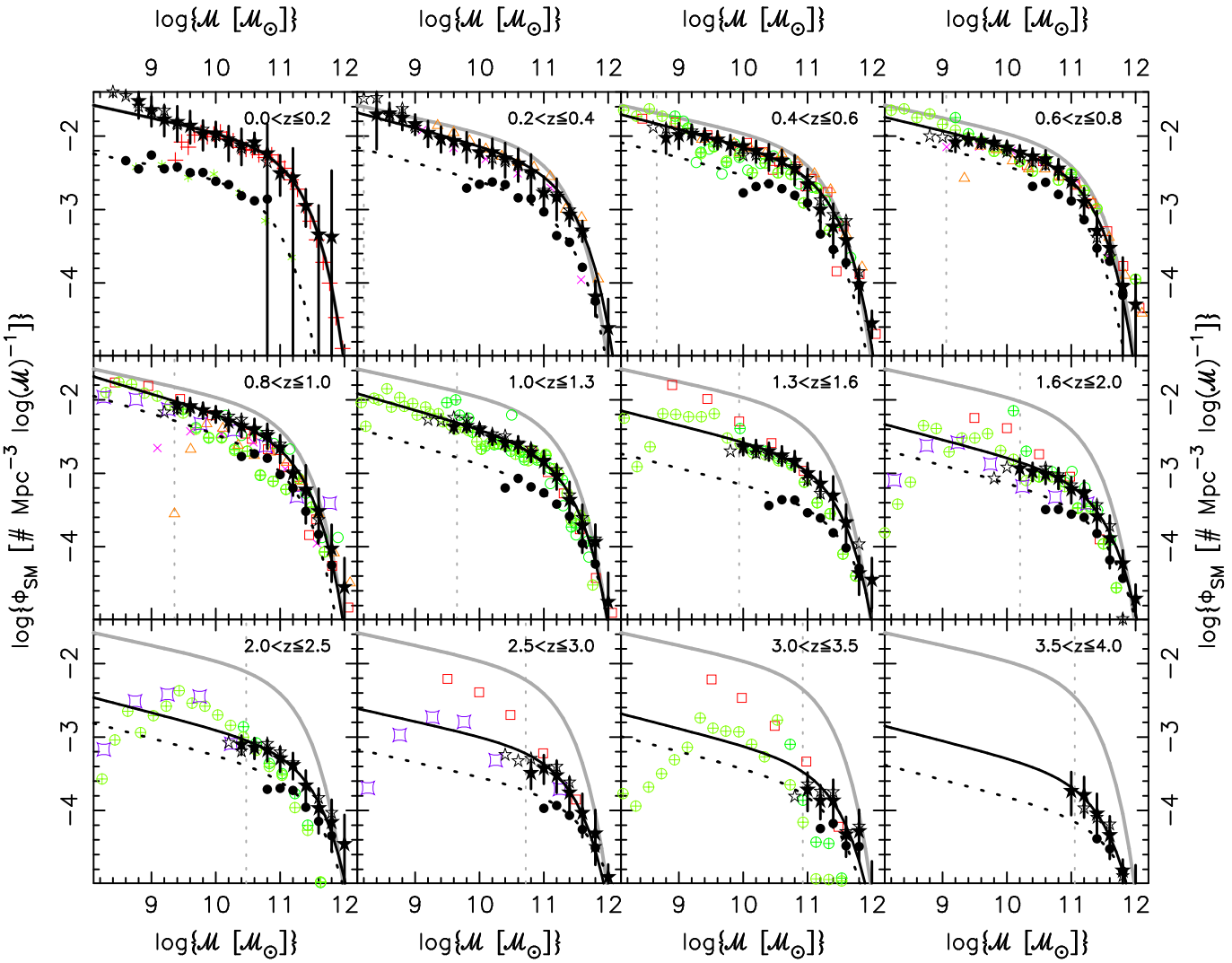

FIG. 6.— Stellar mass functions for 12 redshift intervals from z=0 to z=4. Our estimations at each redshift interval are plotted with black filled stars and errors for the IRAC selected sample, and with open black stars for the *I*-band selected sample (errors for this sample are not plotted for clarity). Filled circles show the SMF for galaxies detected by MIPS at 24 μm. The SMF data (our estimations and others) are fitted with a Schechter (1976) function (black continuous line for the global SMF, and dashed line for the SMF for 24 μm sources). All panels show the local SMF from Cole et al. (2001) with a gray curve. The vertical dotted line shows our 75% completeness limit for the IRAC selected sample. Color points show estimations from other papers: red crosses come from Cole et al. (2001, C01); orange open triangles from Borch et al. (2006, B06); magenta crosses from Pannella et al. (2006); red squares from Drory et al. (2004, D04) and Drory et al. (2005, D05); green crossed circles from Fontana et al. (2003, FC03), Fontana et al. (2004, F04), and Fontana et al. (2006, F06); and purple squares from Conselice et al. (2005, C05). Green asterisks at 0.0<z<0.2 show the stellar mass function of local star-forming galaxies (Pérez-González et al. 2003a, P03).

ies (i.e., mergers accompanied by very little star formation). In addition, given that both in the local Universe and at z∼0.4 the SMFs steepen at low stellar masses ($\mathcal{M}\lesssim10^{9.0}$ $\mathcal{M}_\odot$), the minor merger possibility (accretion of $\mathcal{M}\lesssim10^{9.0}$ $\mathcal{M}_\odot$ galaxies producing very few or even no new stars at all) seem to be the main means of galaxies with $\mathcal{M}=10^{9.0-11.0}$ $\mathcal{M}_\odot$ to increase their stellar mass in the last 4 Gyr.

The evolution in the previous 3–4 Gyr (between z∼1.0 and z∼0.4) was slightly slower. About 25% of the local stellar mass density was assembled in that period, adding up a total decrease of about 50% in the stellar mass density from z=0 to z=1.

At z∼1.0 (8 Gyr ago), the evolution of the stellar mass density of the Universe becomes faster (approximately a factor of 2), just when the cosmic SFR density reaches a maximum (see, e.g., Pérez-González et al. 2005) and the galaxies with $\mathcal{M}\gtrsim10^{10.5}$ $\mathcal{M}_\odot$ dominate the production of stars in the Universe. The rate at which the Universe is creating stars stays at approximately a constant level or decays very slowly from z∼1 up to at least z∼ 2 (10 Gyr ago). Between z∼1 and z∼2, the density of galaxies with $\mathcal{M}\gtrsim10^{10.5}$ $\mathcal{M}_\odot$ decreases significantly (by a factor of 3–4). This population of galaxies evolving rapidly at 1<z<2 (in about 2 Gyr) seem to be dominated by early-type objects (see, e.g., Abraham et al. 2006)

Beyond z∼2, the errors in the stellar mass density estimates and the differences between the observed and extrapolated values become increasingly larger. We find

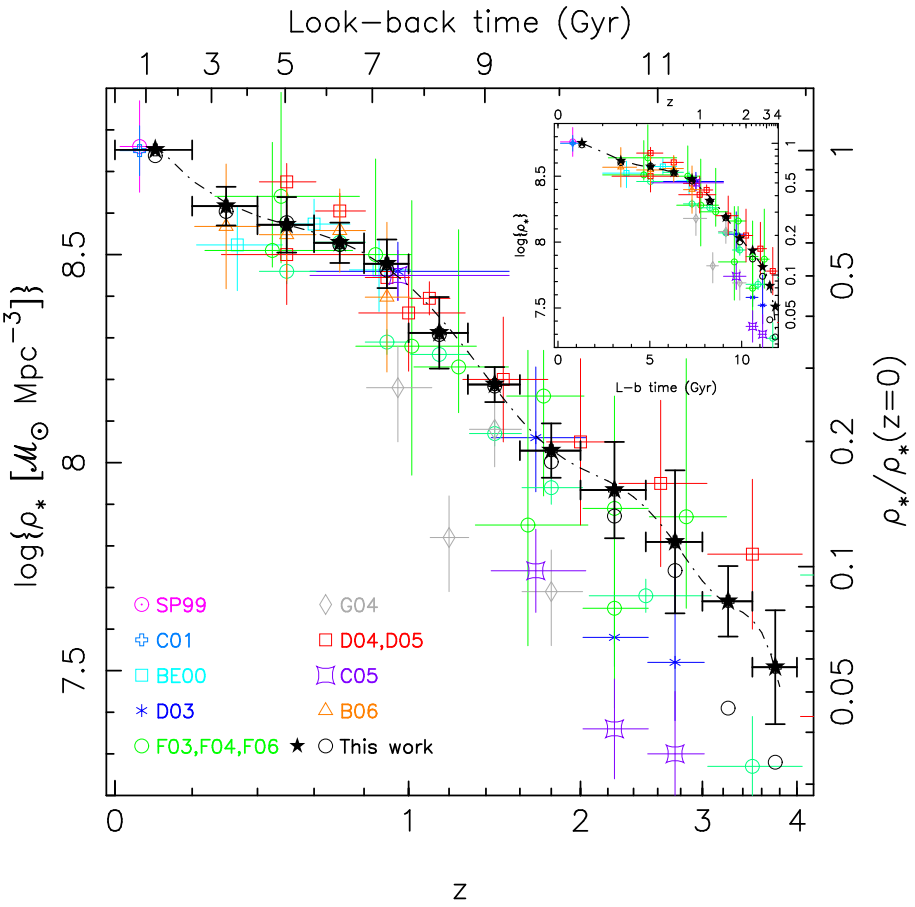

FIG. 7.— Evolution of the stellar mass density of the Universe as function of redshift (shown with a logarithmic scale in the quantity 1+z in the bottom horizontal axis and the corresponding look-back times in the top axis). Our estimations are plotted with black filled stars (based on the integration of the stellar mass functions with a Schechter parametrization) and open circles (observed values down to the completeness level), and fitted to a Chebyshev polynomial with variable (1+z) and $8^{\rm th}$ order (dot-dashed line). Color points and error bars show other estimations found in the literature. To the references mentioned in the caption of Figure 6, we have also added estimations from Salucci & Persic (1999, SP99), Brinchmann & Ellis (2000, BE00), Dickinson et al. (2003b, D03), and Glazebrook et al. (2004, G04). The inset shows the same evolution of the stellar mass density of the Universe, but this time with a linear scale in look-back time in the horizontal axis.

that the rate at which stars are being formed remains constant or even increases slightly, while the giant galaxies with $\mathcal{M}\sim10^{12.0}$ $\mathcal{M}_\odot$ are finishing the assembly of most of their stellar mass.

The different steps in the assembly of the cosmic stellar mass density shown in Figure 7 are consistent with the latest results on the evolution of the observed UV luminosity density of the Universe up to z∼5 (Tresse et al. 2006), which present a maximum at around z=1.2 (with a value approximately 6 times larger than the local UV luminosity density), decrease slightly (by a factor of 1.5) from z=1.2 to z∼2, and increase again up to z∼4. Moreover, a very similar evolution is observed in the cosmic SFR density obtained with IR *Spitzer*/MIPS observations up to z∼2.5 (Pérez-González et al. 2005), and also UV and sub-mm/radio observations up to z∼5 (see Hopkins & Beacom 2006). Our results are also consistent with the hydrodynamical models of Nagamine et al. (2006), which predict that ∼60% of the present stellar mass density was already formed by z=1. However, the discrepancy is significant at z>1, where these models predict a larger stellar mass density than any observation (i.e., they predict a quicker formation of the most massive galaxies). The semi-analytic models of Cole et al. (2000) match our results better at z=3–4, where they predict a stellar mass density of about 10% the present value.

5.6. *Quantifying "downsizing"*

The previous discussion about the evolution of the cosmic stellar mass density is clearly consistent with a "downsizing" scenario for galaxy formation. We quantify some properties of this "downsizing" theory in Figure 8, were we plot the fraction of the total local stellar mass density already assembled in galaxies of a given stellar mass at each redshift. This Figure shows that the most massive systems ($\mathcal{M}\gtrsim10^{12.0}$ $\mathcal{M}_\odot$, orange wider continuous line) formed first (they assembled more than 80% of their total stellar mass before z=3) and very rapidly (about 40% of their mass was assembled in 1 Gyr between z=4 and z=3). Systems with masses $10^{11.7}<\mathcal{M}<10^{12.0}$ $\mathcal{M}_\odot$ assembled their stellar mass more slowly: from z∼4 to z∼2.5 (1.5 Gyr), they assembled around 50% of their stars, and then evolved slowly to reach the local density at low redshift. Less massive

Table 2. Stellar mass functions for the global and star-forming population of galaxies.

Redshift range	$\log(\mathcal{M})^a$	$\log(\phi_{\rm IRAC})^b$	$\log(\phi_{\rm I-band})^b$	$\log(\phi_{\rm MIPS})^b$
$0.0 < z < 0.2$	7.8	$-0.987^{+0.099}_{-0.108}$	$-1.070^{+0.082}_{-0.088}$	...
	8.0	$-1.124^{+0.109}_{-0.119}$	$-1.197^{+0.105}_{-0.115}$	...
	8.2	$-1.142^{+0.109}_{-0.119}$	$-1.275^{+0.101}_{-0.109}$	...
	8.4	$-1.239^{+0.131}_{-0.146}$	$-1.402^{+0.172}_{-0.198}$	...
	8.6	$-1.321^{+0.133}_{-0.148}$	$-1.456^{+0.140}_{-0.156}$	$-2.337^{+0.043}_{-0.047}$
	8.8	$-1.527^{+0.199}_{-0.235}$	$-1.598^{+0.159}_{-0.181}$	$-2.449^{+0.039}_{-0.042}$
	9.0	$-1.650^{+0.187}_{-0.218}$	$-1.680^{+0.255}_{-0.318}$	$-2.259^{+0.045}_{-0.051}$
	9.2	$-1.777^{+0.194}_{-0.227}$	$-1.653^{+0.127}_{-0.141}$	$-2.445^{+0.064}_{-0.075}$
	9.4	$-1.813^{+0.218}_{-0.262}$	$-1.842^{+0.132}_{-0.147}$	$-2.419^{+0.063}_{-0.074}$
	9.6	$-1.862^{+0.202}_{-0.240}$	$-1.862^{+0.159}_{-0.181}$	$-2.498^{+0.067}_{-0.080}$
	9.8	$-1.976^{+0.188}_{-0.219}$	$-1.913^{+0.121}_{-0.133}$	$-2.496^{+0.086}_{-0.107}$
	10.0	$-1.966^{+0.160}_{-0.182}$	$-1.997^{+0.178}_{-0.206}$	$-2.617^{+0.079}_{-0.096}$
	10.2	$-2.081^{+0.216}_{-0.259}$	$-2.041^{+0.086}_{-0.092}$	$-2.662^{+0.063}_{-0.074}$
	10.4	$-2.125^{+0.224}_{-0.270}$	$-2.166^{+0.283}_{-0.362}$	$-2.813^{+0.075}_{-0.091}$
	10.6	$-2.089^{+0.134}_{-0.149}$	$-2.157^{+0.207}_{-0.246}$	$-2.882^{+0.073}_{-0.088}$
	10.8	$-2.237^{+0.400}_{-9.999}$	$-2.355^{+0.205}_{-0.243}$	$-2.858^{+0.052}_{-0.059}$
	11.0	$-2.508^{+0.246}_{-0.304}$	...	...
	11.2	$-2.566^{+0.400}_{-9.999}$	...	...
	11.4	$-2.952^{+0.230}_{-0.280}$	...	...
	11.6	$-3.343^{+0.400}_{-9.999}$	...	...
	11.8	$-3.374^{+0.904}_{-9.999}$	...	...
$0.2 < z < 0.4$	8.2	$-1.748^{+0.388}_{-0.555}$	$-1.491^{+0.123}_{-0.135}$	...
	8.4	$-1.709^{+0.345}_{-0.471}$	$-1.481^{+0.110}_{-0.121}$	...
	8.6	$-1.693^{+0.145}_{-0.163}$	$-1.726^{+0.172}_{-0.198}$	...
	8.8	$-1.754^{+0.146}_{-0.165}$	$-1.631^{+0.129}_{-0.143}$	...
	9.0	$-1.839^{+0.133}_{-0.148}$	$-1.883^{+0.170}_{-0.196}$	...
	9.2	$-1.960^{+0.165}_{-0.189}$	$-1.964^{+0.172}_{-0.198}$	...
	9.4	$-2.035^{+0.164}_{-0.187}$	$-2.048^{+0.218}_{-0.262}$	...
	9.6	$-2.072^{+0.159}_{-0.181}$	$-2.063^{+0.195}_{-0.229}$	...
	9.8	$-2.139^{+0.191}_{-0.224}$	$-2.131^{+0.183}_{-0.212}$	$-2.709^{+0.084}_{-0.104}$
	10.0	$-2.222^{+0.174}_{-0.202}$	$-2.232^{+0.201}_{-0.237}$	$-2.655^{+0.086}_{-0.107}$
	10.2	$-2.222^{+0.186}_{-0.217}$	$-2.301^{+0.167}_{-0.192}$	$-2.626^{+0.070}_{-0.083}$
	10.4	$-2.307^{+0.213}_{-0.255}$	$-2.346^{+0.207}_{-0.247}$	$-2.662^{+0.096}_{-0.123}$
	10.6	$-2.377^{+0.205}_{-0.243}$	$-2.401^{+0.202}_{-0.239}$	$-2.840^{+0.092}_{-0.117}$
	10.8	$-2.493^{+0.243}_{-0.299}$	$-2.519^{+0.202}_{-0.240}$	$-2.854^{+0.086}_{-0.107}$
	11.0	$-2.774^{+0.222}_{-0.268}$	$-2.743^{+0.189}_{-0.221}$	$-3.033^{+0.080}_{-0.098}$
	11.2	$-2.832^{+0.252}_{-0.313}$	$-2.793^{+0.263}_{-0.330}$	$-3.354^{+0.106}_{-0.141}$
	11.4	$-3.073^{+0.138}_{-0.154}$	$-3.011^{+0.196}_{-0.231}$	$-3.447^{+0.089}_{-0.112}$
	11.6	$-3.289^{+0.135}_{-0.150}$	$-3.315^{+0.400}_{-9.999}$	$-3.785^{+3.785}_{-3.785}$
	11.8	$-4.189^{+0.219}_{-0.264}$	...	$-4.248^{+4.248}_{-4.248}$
	12.0	$-4.616^{+0.400}_{-5.374}$	...	...

Note. — [a] In units of $\mathcal{M}_\odot$. [b] In units of $\mathrm{Mpc}^{-3}\,(\log\mathcal{M})^{-1}$.

galaxies assembled their mass at even a slower speed, reaching the local density at very recent epochs. Again, this plot shows the rapid recent evolution of the galaxies with masses $\mathcal{M}\sim10^{10.5}$ $\mathcal{M}_\odot$, which assembled $\sim$40% of their mass in the last 3 Gyr. The "downsizing" scenario is also confirmed by the distribution of median ages (estimated from our stellar population models) as a function of stellar mass. We find that the median age and quartiles for galaxies with $\mathcal{M}<10^{8.0}$ $\mathcal{M}_\odot$ are $\log(t/yr) = 8.0^{9.2}_{7.0}$, for $10^{8.0}<\mathcal{M}<10^{9.0}$ $\mathcal{M}_\odot$ $\log(t/yr) = 8.3^{9.2}_{7.5}$, for $10^{9.0}<\mathcal{M}<10^{10.0}$ $\mathcal{M}_\odot$ $\log(t/yr) = 8.9^{9.3}_{8.1}$, for $10^{10.0}<\mathcal{M}<10^{11.0}$ $\mathcal{M}_\odot$ $\log(t/yr) = 9.1^{9.4}_{8.5}$, for $10^{11.0}<\mathcal{M}<10^{11.5}$ $\mathcal{M}_\odot$ $\log(t/yr) = 9.2^{9.5}_{9.0}$, and for $\mathcal{M}>10^{11.5}$ $\mathcal{M}_\odot$ $\log(t/yr) = 9.1^{9.3}_{8.7}$. Note that for the most massive galaxies, formed at higher redshifts, the age of the Universe is very similar to the derived stellar population ages, i.e., the age of the Universe is a strong constrain for the most massive systems.

Our results are consistent with the stellar population models assumed by Brown et al. (2007) for the most luminous (and probably most massive) red galaxies. According to this paper, red massive galaxies start forming at an early epoch, at z=4, following an exponential SF law with a short τ=0.6 Gyr. Jimenez et al. (2006) find that the most massive early-type galaxies in the local Universe formed at z>2.5 and experienced a very

TABLE 2. STELLAR MASS FUNCTIONS FOR THE GLOBAL AND STAR-FORMING POPULATION OF GALAXIES.

Redshift range	$\log(\mathcal{M})^a$	$\log(\phi_{\rm IRAC})^b$	$\log(\phi_{\rm I-band})^b$	$\log(\phi_{\rm MIPS})^b$
$0.4 < z < 0.6$	8.6	...	$-1.882^{+0.193}_{-0.226}$	...
	8.8	$-2.028^{+0.183}_{-0.212}$	$-1.898^{+0.184}_{-0.214}$	...
	9.0	$-1.989^{+0.166}_{-0.190}$	$-1.933^{+0.151}_{-0.171}$	...
	9.2	$-1.972^{+0.126}_{-0.140}$	$-1.937^{+0.142}_{-0.160}$	...
	9.4	$-2.003^{+0.107}_{-0.117}$	$-1.994^{+0.160}_{-0.182}$	...
	9.6	$-2.052^{+0.117}_{-0.129}$	$-2.085^{+0.177}_{-0.205}$	...
	9.8	$-2.116^{+0.128}_{-0.142}$	$-2.120^{+0.170}_{-0.195}$	...
	10.0	$-2.139^{+0.117}_{-0.129}$	$-2.264^{+0.189}_{-0.221}$	$-2.773^{+0.070}_{-0.084}$
	10.2	$-2.205^{+0.140}_{-0.157}$	$-2.256^{+0.192}_{-0.226}$	$-2.688^{+0.069}_{-0.082}$
	10.4	$-2.278^{+0.168}_{-0.193}$	$-2.263^{+0.182}_{-0.211}$	$-2.650^{+0.066}_{-0.077}$
	10.6	$-2.340^{+0.153}_{-0.173}$	$-2.329^{+0.204}_{-0.242}$	$-2.716^{+0.066}_{-0.078}$
	10.8	$-2.449^{+0.188}_{-0.219}$	$-2.420^{+0.209}_{-0.249}$	$-2.808^{+0.072}_{-0.086}$
	11.0	$-2.661^{+0.214}_{-0.257}$	$-2.579^{+0.254}_{-0.316}$	$-2.914^{+0.074}_{-0.089}$
	11.2	$-3.003^{+0.270}_{-0.340}$	$-2.874^{+0.245}_{-0.302}$	$-3.335^{+0.093}_{-0.118}$
	11.4	$-3.236^{+0.316}_{-0.419}$	$-3.073^{+0.252}_{-0.313}$	$-3.544^{+0.127}_{-0.181}$
	11.6	$-3.419^{+0.293}_{-0.378}$	$-3.158^{+0.292}_{-0.378}$	$-3.721^{+0.064}_{-0.075}$
	11.8	$-4.022^{+0.213}_{-0.254}$	$-3.850^{+0.400}_{-9.999}$	$-4.029^{+0.122}_{-0.169}$
	12.0	$-4.551^{+0.173}_{-0.199}$	...	...
$0.6 < z < 0.8$	8.8	...	$-2.000^{+0.134}_{-0.149}$	...
	9.0	...	$-2.018^{+0.126}_{-0.139}$	...
	9.2	$-2.090^{+0.117}_{-0.128}$	$-2.032^{+0.119}_{-0.131}$	...
	9.4	$-2.048^{+0.081}_{-0.086}$	$-2.065^{+0.131}_{-0.145}$	...
	9.6	$-2.067^{+0.092}_{-0.099}$	$-2.097^{+0.146}_{-0.165}$	...
	9.8	$-2.092^{+0.088}_{-0.095}$	$-2.126^{+0.148}_{-0.167}$	...
	10.0	$-2.161^{+0.094}_{-0.101}$	$-2.216^{+0.147}_{-0.165}$	...
	10.2	$-2.227^{+0.103}_{-0.112}$	$-2.314^{+0.177}_{-0.204}$	...
	10.4	$-2.281^{+0.112}_{-0.123}$	$-2.357^{+0.159}_{-0.182}$	$-2.685^{+0.057}_{-0.066}$
	10.6	$-2.319^{+0.124}_{-0.137}$	$-2.394^{+0.172}_{-0.199}$	$-2.631^{+0.059}_{-0.068}$
	10.8	$-2.445^{+0.131}_{-0.146}$	$-2.473^{+0.194}_{-0.228}$	$-2.795^{+0.067}_{-0.079}$
	11.0	$-2.623^{+0.164}_{-0.187}$	$-2.590^{+0.196}_{-0.231}$	$-2.883^{+0.065}_{-0.077}$
	11.2	$-2.902^{+0.192}_{-0.226}$	$-2.833^{+0.190}_{-0.222}$	$-3.139^{+0.088}_{-0.111}$
	11.4	$-3.293^{+0.273}_{-0.345}$	$-3.381^{+0.162}_{-0.185}$	$-3.529^{+0.080}_{-0.099}$
	11.6	$-3.525^{+0.163}_{-0.187}$	$-3.648^{+0.105}_{-0.114}$	$-3.704^{+3.704}_{-3.704}$
	11.8	$-4.052^{+0.400}_{-9.999}$	$-4.032^{+0.324}_{-0.433}$	$-4.169^{+4.169}_{-4.169}$
	12.0	$-4.297^{+0.405}_{-9.999}$	...	...

Note. — [a] In units of $\mathcal{M}_\odot$. [b] In units of $\mathrm{Mpc}^{-3}\,(\log\mathcal{M})^{-1}$.

rapid chemical enrichment, lasting 1-2 Gyr. Also van der Wel et al. (2005) find signs of the formation of massive ($\mathcal{M}>2\times10^{11}$ $\mathcal{M}_\odot$, according to these authors) early-type galaxies at $z\gtrsim2$, while less massive systems present lower formation redshifts ($1<z<2$). The analysis of optical spectra for spheroidal and bulge-dominated galaxies at $0.2<z<1.2$ by Treu et al. (2005) also reveals that most of the mass (99%) in systems with $\mathcal{M}>10^{11.5}$ $\mathcal{M}_\odot$ formed at $z>2$, while most recent bursts (at $z\sim1.2$) can account for 20%-40% of the total stellar mass of galaxies with $\mathcal{M}<10^{11.0}$ $\mathcal{M}_\odot$. Glazebrook et al. (2004) estimates that 38±18% of the stellar mass density in galaxies with $\mathcal{M}>10^{10.8}$ $\mathcal{M}_\odot$ were already in place at $z=1$, consistent with our value of ∼45%. At $z=1.8$, Glazebrook et al. (2004) obtain 16±6%, also in agreement with our own estimation of ∼21%.

If we consider a high value of the fraction of the stellar mass density already assembled at a given redshift, above which the star formation in a galaxy should be relatively low, e.g., 80%, Figure 8 shows that galaxies with $\mathcal{M}\sim10^{10.5}$ $\mathcal{M}_\odot$ reached that level at $z\sim0.2$, systems with $\mathcal{M}\sim10^{11.25}$ $\mathcal{M}_\odot$ at $z\sim0.4$, and galaxies with $\mathcal{M}\sim10^{11.75}$ $\mathcal{M}_\odot$ around $z\sim0.7$. These numbers are roughly consistent with the $(1+z)^{3.5}$ evolution estimated by Bundy et al. (2006) for the quenching stellar mass ($\mathcal{M}_{\rm Q}$), a mass limit above which the star formation appears to be suppressed.

According to Figure 8, 50% of the stars in galaxies with $\mathcal{M}>10^{11.0}$ $\mathcal{M}_\odot$ were already in place at $z\sim0.9$. This compares well with the prediction from the models in De Lucia et al. (2006) which establish that half of the stars in objects of this mass are assembled into single objects at $z\sim0.8$. However, these models also predict that most of these stars were already formed at $z\sim2.5$, but were placed in several objects that would coalesce into a single object later. This hierarchical scenario could be reconciled with our results if the global production of stars in systems with $\mathcal{M}>10^{11.0}$ $\mathcal{M}_\odot$ is dominated by the most massive

Table 2. Stellar mass functions for the global and star-forming population of galaxies.

Redshift range	$\log(\mathcal{M})^a$	$\log(\phi_{\rm IRAC})^b$	$\log(\phi_{\rm I-band})^b$	$\log(\phi_{\rm MIPS})^b$
$0.8 < z < 1.0$	9.2	...	$-2.170^{+0.213}_{-0.254}$	...
	9.4	$-2.073^{+0.107}_{-0.116}$	$-2.123^{+0.192}_{-0.225}$	...
	9.6	$-2.089^{+0.116}_{-0.127}$	$-2.111^{+0.164}_{-0.188}$	...
	9.8	$-2.145^{+0.104}_{-0.114}$	$-2.145^{+0.144}_{-0.162}$	...
	10.0	$-2.195^{+0.109}_{-0.118}$	$-2.181^{+0.167}_{-0.192}$	...
	10.2	$-2.300^{+0.122}_{-0.134}$	$-2.226^{+0.141}_{-0.159}$	...
	10.4	$-2.361^{+0.131}_{-0.146}$	$-2.270^{+0.162}_{-0.185}$	$-2.771^{+0.056}_{-0.064}$
	10.6	$-2.400^{+0.141}_{-0.158}$	$-2.409^{+0.188}_{-0.220}$	$-2.735^{+0.052}_{-0.060}$
	10.8	$-2.485^{+0.159}_{-0.181}$	$-2.446^{+0.223}_{-0.269}$	$-2.795^{+0.053}_{-0.060}$
	11.0	$-2.656^{+0.176}_{-0.203}$	$-2.608^{+0.210}_{-0.251}$	$-3.019^{+0.072}_{-0.087}$
	11.2	$-3.006^{+0.243}_{-0.299}$	$-2.987^{+0.198}_{-0.234}$	$-3.203^{+0.086}_{-0.107}$
	11.4	$-3.227^{+0.337}_{-0.456}$	$-3.249^{+0.155}_{-0.176}$	$-3.517^{+0.101}_{-0.132}$
	11.6	$-3.519^{+0.311}_{-0.409}$	$-3.635^{+0.172}_{-0.198}$	$-3.832^{+0.087}_{-0.109}$
	11.8	$-4.031^{+0.332}_{-0.446}$	$-4.028^{+1.189}_{-0.528}$	$-4.250^{+4.250}_{-4.250}$
	12.0	$-4.553^{+0.400}_{-5.437}$	...	...
$1.0 < z < 1.3$	9.2	...	$-2.271^{+0.167}_{-0.192}$	...
	9.4	...	$-2.286^{+0.173}_{-0.199}$	...
	9.6	$-2.370^{+0.083}_{-0.088}$	$-2.245^{+0.126}_{-0.139}$	...
	9.8	$-2.359^{+0.079}_{-0.084}$	$-2.268^{+0.132}_{-0.147}$	...
	10.0	$-2.409^{+0.082}_{-0.087}$	$-2.387^{+0.138}_{-0.154}$	...
	10.2	$-2.514^{+0.095}_{-0.102}$	$-2.467^{+0.157}_{-0.178}$	...
	10.4	$-2.587^{+0.103}_{-0.112}$	$-2.494^{+0.151}_{-0.170}$	$-3.199^{+0.063}_{-0.073}$
	10.6	$-2.606^{+0.111}_{-0.122}$	$-2.591^{+0.172}_{-0.199}$	$-3.071^{+0.056}_{-0.064}$
	10.8	$-2.719^{+0.117}_{-0.128}$	$-2.661^{+0.180}_{-0.209}$	$-3.186^{+0.065}_{-0.076}$
	11.0	$-2.840^{+0.145}_{-0.163}$	$-2.827^{+0.207}_{-0.246}$	$-3.266^{+0.074}_{-0.090}$
	11.2	$-3.040^{+0.159}_{-0.182}$	$-2.956^{+0.209}_{-0.249}$	$-3.420^{+0.072}_{-0.087}$
	11.4	$-3.365^{+0.249}_{-0.308}$	$-3.298^{+0.162}_{-0.185}$	$-3.586^{+0.091}_{-0.115}$
	11.6	$-3.714^{+0.288}_{-0.370}$	$-3.608^{+0.267}_{-0.336}$	$-3.955^{+0.106}_{-0.141}$
	11.8	$-3.937^{+0.239}_{-0.292}$	$-3.899^{+0.400}_{-9.999}$	$-4.237^{+0.138}_{-0.204}$
	12.0	$-4.754^{+0.400}_{-5.326}$	$-4.295^{+0.400}_{-5.753}$	...
$1.3 < z < 1.6$	9.8	...	$-2.700^{+0.183}_{-0.212}$	...
	10.0	$-2.634^{+0.111}_{-0.122}$	$-2.659^{+0.154}_{-0.175}$	...
	10.2	$-2.658^{+0.111}_{-0.121}$	$-2.728^{+0.305}_{-0.398}$	...
	10.4	$-2.701^{+0.116}_{-0.127}$	$-2.746^{+0.161}_{-0.184}$	$-3.440^{+0.075}_{-0.091}$
	10.6	$-2.758^{+0.126}_{-0.139}$	$-2.792^{+0.148}_{-0.168}$	$-3.360^{+0.074}_{-0.089}$
	10.8	$-2.831^{+0.133}_{-0.148}$	$-2.854^{+0.149}_{-0.169}$	$-3.364^{+0.072}_{-0.086}$
	11.0	$-3.002^{+0.143}_{-0.160}$	$-3.092^{+0.242}_{-0.298}$	$-3.538^{+0.088}_{-0.111}$
	11.2	$-3.144^{+0.167}_{-0.192}$	$-3.276^{+0.239}_{-0.293}$	$-3.608^{+0.090}_{-0.113}$
	11.4	$-3.304^{+0.262}_{-0.328}$	$-3.304^{+0.227}_{-0.275}$	$-3.811^{+0.101}_{-0.132}$
	11.6	$-3.674^{+0.248}_{-0.307}$	$-3.662^{+0.202}_{-0.239}$	$-4.016^{+0.089}_{-0.111}$
	11.8	$-4.364^{+0.237}_{-0.291}$	$-3.965^{+0.095}_{-0.103}$	$-4.292^{+0.056}_{-0.065}$
	12.0	$-4.451^{+0.299}_{-0.388}$	...	...

Note. — ^{a} In units of $\mathcal{M}_\odot$. ^{b} In units of $\mathrm{Mpc}^{-3}\,(\log\mathcal{M})^{-1}$.

systems with $\mathcal{M}\gtrsim10^{12.0}\,\mathcal{M}_\odot$, which formed most of their mass at z>2.5 (50% of their mass would be assembled by z∼4 according to Nagamine et al. 2005b, in agreement with Figure 8) and assembled very rapidly (in a way closer to a monolithic collapse than to a hierarchical coalescence), but less massive systems formed their stars later and/or assembled half of their mass from several progenitors in the time interval between z∼2.5 and z∼1 (about 4 Gyr), and most of their mass (80%) not before z∼0.5. To confirm this scenario, it would be necessary to probe the stellar mass function at low masses (for objects that would act as building blocks for the galaxies with $\mathcal{M}\gtrsim10^{11.0}\,\mathcal{M}_\odot$), but the scatter of the currently available SMF estimations at low masses in this redshift range is too large to obtain robust results (maybe due to cosmic variance effects). Indeed, our estimations of the cosmic stellar mass density at z>3 are affected by the large uncertainties at masses below $10^{11}\,\mathcal{M}_\odot$ (this explains the large difference between the observed and extrapolated values of the density at z>3). The dual galaxy formation scenario (quasi-monolithic and rapid collapse of the most massive galaxies which cease to form stars at a certain epoch, and hierarchical collapse for less massive systems) has been reproduced by other models where AGNs are

TABLE 2. STELLAR MASS FUNCTIONS FOR THE GLOBAL AND STAR-FORMING POPULATION OF GALAXIES.

Redshift range	$\log(\mathcal{M})^a$	$\log(\phi_{\rm IRAC})^b$	$\log(\phi_{\rm I-band})^b$	$\log(\phi_{\rm MIPS})^b$
$1.6 < z < 2.0$	9.8	...	$-3.071^{+0.261}_{-0.327}$	...
	10.0	...	$-2.920^{+0.199}_{-0.235}$	...
	10.2	$-2.936^{+0.138}_{-0.154}$	$-2.931^{+0.266}_{-0.335}$	...
	10.4	$-2.975^{+0.118}_{-0.130}$	$-2.986^{+0.251}_{-0.311}$	...
	10.6	$-3.014^{+0.120}_{-0.132}$	$-2.932^{+0.236}_{-0.288}$	$-3.494^{+0.069}_{-0.082}$
	10.8	$-3.063^{+0.136}_{-0.152}$	$-3.024^{+0.280}_{-0.357}$	$-3.492^{+0.063}_{-0.074}$
	11.0	$-3.218^{+0.167}_{-0.192}$	$-3.161^{+0.227}_{-0.276}$	$-3.555^{+0.090}_{-0.114}$
	11.2	$-3.271^{+0.168}_{-0.193}$	$-3.250^{+0.304}_{-0.398}$	$-3.598^{+0.067}_{-0.080}$
	11.4	$-3.588^{+0.194}_{-0.227}$	$-3.433^{+0.210}_{-0.251}$	$-3.819^{+0.098}_{-0.126}$
	11.6	$-3.886^{+0.310}_{-0.407}$	$-3.720^{+0.189}_{-0.222}$	$-4.180^{+0.114}_{-0.155}$
	11.8	$-4.229^{+0.179}_{-0.208}$	$-4.983^{+2.866}_{-2.510}$	$-4.429^{+0.061}_{-0.071}$
	12.0	$-4.711^{+0.196}_{-0.231}$	$-4.232^{+0.204}_{-0.242}$	...
$2.0 < z < 2.5$	10.2	...	$-3.077^{+0.209}_{-0.249}$	...
	10.4	$-3.105^{+0.125}_{-0.138}$	$-3.193^{+0.219}_{-0.263}$	...
	10.6	$-3.148^{+0.135}_{-0.151}$	$-3.101^{+0.335}_{-0.452}$	...
	10.8	$-3.178^{+0.138}_{-0.154}$	$-3.091^{+0.208}_{-0.247}$	$-3.712^{+0.068}_{-0.080}$
	11.0	$-3.292^{+0.159}_{-0.182}$	$-3.208^{+0.211}_{-0.251}$	$-3.698^{+0.071}_{-0.085}$
	11.2	$-3.384^{+0.167}_{-0.191}$	$-3.355^{+0.185}_{-0.215}$	$-3.727^{+0.067}_{-0.079}$
	11.4	$-3.662^{+0.205}_{-0.244}$	$-3.663^{+0.283}_{-0.362}$	$-3.955^{+0.087}_{-0.108}$
	11.6	$-3.971^{+0.271}_{-0.342}$	$-3.829^{+0.214}_{-0.257}$	$-4.148^{+0.084}_{-0.105}$
	11.8	$-4.160^{+0.306}_{-0.401}$	$-4.031^{+0.274}_{-0.347}$	$-4.343^{+0.083}_{-0.103}$
	12.0	$-4.460^{+0.400}_{-5.530}$	...	...
$2.5 < z < 3.0$	10.4	...	$-3.243^{+0.208}_{-0.248}$	...
	10.6	...	$-3.327^{+0.197}_{-0.232}$	...
	10.8	$-3.492^{+0.184}_{-0.215}$	$-3.296^{+0.389}_{-0.558}$	...
	11.0	$-3.428^{+0.181}_{-0.211}$	$-3.405^{+0.194}_{-0.228}$	$-3.970^{+0.075}_{-0.090}$
	11.2	$-3.523^{+0.201}_{-0.238}$	$-3.403^{+0.325}_{-0.434}$	$-3.931^{+0.064}_{-0.075}$
	11.4	$-3.759^{+0.215}_{-0.258}$	$-3.617^{+0.200}_{-0.236}$	$-4.066^{+0.094}_{-0.120}$
	11.6	$-4.035^{+0.263}_{-0.330}$	$-4.032^{+0.198}_{-0.234}$	$-4.258^{+0.099}_{-0.128}$
	11.8	$-4.314^{+0.321}_{-0.427}$	$-4.495^{+0.248}_{-0.306}$	$-4.507^{+0.128}_{-0.181}$
	12.0	$-4.909^{+0.174}_{-0.200}$	$-3.550^{+0.179}_{-0.208}$	...
$3.0 < z < 3.5$	10.8	...	$-3.811^{+1.336}_{-0.991}$	...
	11.0	$-3.719^{+0.236}_{-0.289}$	$-3.642^{+0.467}_{-0.203}$	...
	11.2	$-3.867^{+0.212}_{-0.253}$	$-3.741^{+1.389}_{-0.298}$	$-4.246^{+0.069}_{-0.081}$
	11.4	$-3.867^{+0.286}_{-0.367}$	$-3.748^{+0.110}_{-0.649}$	$-4.177^{+0.096}_{-0.124}$
	11.6	$-4.330^{+0.245}_{-0.302}$	$-4.290^{+0.699}_{-1.009}$	$-4.481^{+0.105}_{-0.139}$
	11.8	$-4.284^{+0.294}_{-0.381}$	$-4.216^{+0.634}_{-2.205}$	$-4.490^{+0.102}_{-0.133}$
	12.0	$-5.090^{+0.400}_{-4.993}$	$-3.847^{+1.621}_{-0.317}$	...
$3.5 < z < 4.0$	11.0	$-3.736^{+0.262}_{-0.328}$	$-3.737^{+0.564}_{-1.017}$	...
	11.2	$-3.791^{+0.249}_{-0.307}$	$-3.967^{+0.191}_{-0.224}$	...
	11.4	$-4.045^{+0.272}_{-0.345}$	$-4.096^{+0.104}_{-0.113}$	$-4.385^{+0.090}_{-0.113}$
	11.6	$-4.338^{+0.259}_{-0.323}$	$-4.188^{+0.160}_{-0.182}$	$-4.523^{+0.093}_{-0.118}$
	11.8	$-4.820^{+0.153}_{-0.173}$	$-4.891^{+0.174}_{-0.201}$	$-4.828^{+0.056}_{-0.064}$
	12.0	$-5.111^{+0.369}_{-0.817}$	...	...

Note. — [a] In units of $\mathcal{M}_\odot$. [b] In units of $\mathrm{Mpc}^{-3}\,(\log\mathcal{M})^{-1}$.

supposed to quench the star formation in very massive halos (see, e.g., Bower et al. 2006; Croton et al. 2006).

It is also interesting to note the change in slope at z∼0.7 of the curves shown in Figure 8. At this redshift, the fraction of the local stellar mass density in galaxies with masses above $10^{11.7}$ $\mathcal{M}_\odot$, which remained almost constant from z∼2.5, rapidly (in ∼1 Gyr) increases a 30% to reach the local value. In contrast, at z∼0.7 (but above z∼0.4) less massive objects ($\mathcal{M}<10^{11.5}$ $\mathcal{M}_\odot$) start to accumulate stellar mass less rapidly than at higher redshifts. At z∼0.4, where the most massive galaxies have already reached the current density, low-mass galaxies start to form again a significant number of their stars at a more rapid rate than at 0.4<z<0.8. Thus, this redshift interval represents an epoch of "upsizing" in the galaxy formation history, probably related to a transition between an epoch dominated by the "downsizing" formation of the spheroids (first the most massive, and then less-massive ones) to an epoch where the also "downsizing" formation of the disks (from high-mass disks first

TABLE 3. RESULTS OF THE SCHECHTER (1976) FITS TO THE GLOBAL AND STAR-FORMING STELLAR MASS FUNCTIONS.

	GLOBAL					STAR-FORMING				
Redshift range	α	$\log(\mathcal{M}^*)^a$	$\log(\phi^*)^b$	$\log(\rho_*)^c$	$\log(\rho_*^{\rm obs})^c$	$\alpha_{\rm SF}$	$\log(\mathcal{M}^*_{\rm SF})^a$	$\log(\phi^*_{\rm SF})^b$	$\log(\rho_*^{\rm SF})^c$	$\log(\rho_*^{\rm obs})^c$
$0.0 < z \leq 0.2$	-1.19±0.13	11.19±0.28	-2.53±0.25	8.74±0.12	8.74	-1.16±0.13	10.84±0.16	-3.05±0.17	7.84±0.07	7.84
$0.2 < z \leq 0.4$	-1.23±0.09	11.33±0.11	-2.80±0.16	8.62±0.05	8.60	-1.23±0.09	11.31±0.08	-3.27±0.06	8.13±0.05	8.10
$0.4 < z \leq 0.6$	-1.22±0.11	11.28±0.16	-2.78±0.20	8.57±0.06	8.58	-1.22±0.11	11.25±0.14	-3.16±0.07	8.17±0.08	8.18
$0.6 < z \leq 0.8$	-1.21±0.11	11.21±0.12	-2.75±0.16	8.53±0.05	8.52	-1.21±0.11	11.11±0.06	-2.97±0.07	8.21±0.03	8.13
$0.8 < z \leq 1.0$	-1.26±0.07	11.25±0.08	-2.87±0.13	8.48±0.06	8.46	-1.26±0.07	11.19±0.08	-3.12±0.07	8.17±0.03	8.13
$1.0 < z \leq 1.3$	-1.25±0.10	11.30±0.19	-3.08±0.19	8.31±0.07	8.31	-1.25±0.10	11.44±0.07	-3.59±0.06	7.94±0.03	7.83
$1.3 < z \leq 1.6$	-1.22±0.08	11.33±0.10	-3.22±0.12	8.19±0.04	8.18	-1.22±0.08	11.52±0.10	-3.84±0.07	7.75±0.05	7.69
$1.6 < z \leq 2.0$	-1.23±0.09	11.42±0.14	-3.47±0.18	8.03±0.06	8.00	-1.23±0.09	11.49±0.05	-3.83±0.08	7.74±0.04	7.71
$2.0 < z \leq 2.5$	-1.23±0.09	11.44±0.25	-3.58±0.22	7.93±0.11	7.87	-1.23±0.09	11.49±0.18	-3.94±0.16	7.63±0.07	7.42
$2.5 < z \leq 3.0$	-1.20±0.28	11.36±0.40	-3.61±0.44	7.81±0.17	7.74	-1.20±0.28	11.64±0.15	-4.22±0.13	7.48±0.07	7.39
$3.0 < z \leq 3.5$	-1.22±0.02	11.37±0.10	-3.78±0.11	7.67±0.09	7.41	-1.22±0.02	11.39±0.31	-4.10±0.36	7.37±0.15	7.25
$3.5 < z \leq 4.0$	-1.22±0.02	11.38±0.11	-3.95±0.23	7.51±0.14	7.28	-1.22±0.02	11.65±0.13	-4.54±0.16	7.19±0.06	6.97

Note. — [a] In units of $\mathcal{M}_\odot$. [b] In units of $\mathrm{Mpc}^{-3}\,(\log\mathcal{M})^{-1}$. [c] In units of $\mathcal{M}_\odot\mathrm{Mpc}^{-3}$.

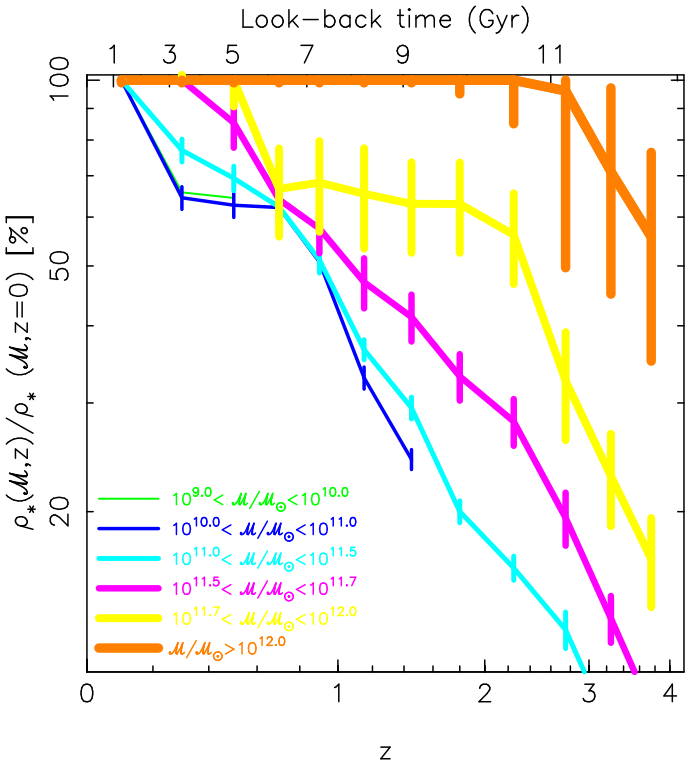

FIG. 8.— Fraction of the local stellar mass density already assembled at a given redshift for several mass intervals (wider lines referring to more massive systems). Only results for masses above our 75% completeness level at each redshift are shown.

to low-mass disks at z<0.4) plays a more important role in terms of formation of stellar mass. In this sense, it is worth recalling here that low-mass disks are the dominant population of star-forming galaxies in the Local Universe (Pérez-González et al. 2001). Note that we are not claiming here that disks started to form at z∼0.7. A simple delay in the formation of disks compared with spheroids of similar mass might result (under the right circumstances) in such transition epoch.

While results supporting the "downsizing" formation scenario in spheroids are numerous (see references above), evidence for "downsizing" in morphologically-classified spiral disks are more limited. A notorious exception is the work of Bundy et al. (2006), where the fraction of the total mass contributed by spirals of different mass is found to significantly evolve from z=1.2, where the largest contributors are spirals with masses above 10^{11} $\mathcal{M}_\odot$, to z=0.5, where low-mass spirals dominate (see their Figure 8).

The "upsizing" supported by the results in Figure 8 would also be consistent with a hierarchical scenario of galaxy formation, where less massive systems form continuously (i.e., their density monotonically increases), and at some time they merge to form larger systems. This could be an explanation for the stop in the evolution of $\mathcal{M}\lesssim 10^{10.5}$ $\mathcal{M}_\odot$ galaxies, whose stellar mass density remains approximately constant from z∼0.8 to z∼0.2, maybe because these galaxies are merging to form larger ones. This would end up in the increase of the stellar mass density in more massive systems, which is actually observed in Figure 8, and in the global increase of the cosmic stellar mass density, which was discussed in Figure 7.

6. THE NATURE OF THE IRAC SAMPLE: COMPARISON WITH OTHER SURVEYS

In this Section, we will discuss the main properties of the sources in our IRAC sample, comparing them with the populations of galaxies detected with different selection techniques by other surveys. The results discussed in this Section are summarized in Tables 4 and 5.

Based on the observed photometric data points and the SED fit for each galaxy in our sample, we estimated observed magnitudes in 9 bands (FUV, NUV, U_n, B, $\mathcal{G}$, $\mathcal{R}$, z, J, and K_s) in order to test which of our galaxies would qualify as Lyman Break Galaxies (LBGs) at z∼1 (GALEX LBGs, Burgarella et al. 2006), at z=1.5–2.5 (LBG-BM and LBG-BX galaxies in Steidel et al. 2004), and at z∼3 ("classical" LBGs, Steidel et al. 2003), and which of our galaxies would qualify as Distant Red Galaxies (DRGs; Franx et al. 2003; van Dokkum et al. 2003) or BzK sources (Daddi et al. 2004).

Table 4. The IRAC sample: Comparison with other surveys.

	Number of sources/MIPS detections								Number of sources			
	IRAC[a]	LBG[b]				DRG[a]	BzK[a]		LBG[b]	DRG[a]	BzK[a]	JUST
Redshift		GALEX	BM	BX	"classic"		PE	SF	DRG[a]	BzK[a]	LBG[b]	IRAC[a,c]
(0.0, 0.2]	1473/242	0/0	81/11	510/94	2/0	9/4	0/0	468/62	3	9	243	655
(0.2, 0.4]	1745/375	0/0	121/10	183/30	5/0	8/1	0/0	318/54	1	8	134	1252
(0.4, 0.6]	2473/660	0/0	26/1	6/1	9/1	37/4	1/0	303/39	1	32	29	2152
(0.6, 0.8]	3953/979	0/0	55/2	6/0	1/0	38/9	2/1	403/55	1	27	39	3514
(0.8, 1.0]	4226/1065	300/117	273/43	12/2	0/0	78/28	2/0	508/109	7	46	192	3314
(1.0, 1.3]	4140/1012	189/66	1100/189	117/25	1/1	118/48	21/5	1060/130	13	87	540	2233
(1.3, 1.6]	2040/619	0/0	817/213	141/48	5/2	61/26	105/32	1458/439	2	58	804	315
(1.6, 2.0]	1640/532	0/0	414/105	412/129	24/8	55/18	104/33	1417/468	8	55	821	90
(2.0, 2.5]	1404/439	0/0	144/39	551/154	95/29	231/109	49/17	1274/406	43	230	762	52
(2.5, 3.0]	882/264	0/0	4/0	135/31	278/82	253/127	23/15	677/197	59	234	322	68
(3.0, 3.5]	558/162	0/0	0/0	1/1	365/85	171/93	15/10	294/104	49	144	194	52
(3.5, 4.0]	529/95	0/0	0/0	4/0	276/36	165/59	33/20	115/23	40	102	65	117

Note. — [a] Any magnitude. [b] Magnitude limited to R<25.5. [c] IRAC sources not recovered by any other selection criteria (i.e., they are not LBGs, DRGs, or BzK galaxies).

We identified LBGs following Steidel et al. (2003) and Steidel et al. (2004), which establish the locus of LBGs in a $Un-\mathcal{G}$ vs. $\mathcal{G}-\mathcal{R}$ color-color diagram, and the magnitude cut (R<25.5) for their survey. We identified GALEX LBGs with an analog procedure, but this time using a color criteria based on GALEX UV photometric bands (see Burgarella et al. 2006). Following Franx et al. (2003), we defined DRGs as the galaxies presenting a color $J-K_s$>1.37 [corresponding to $(J-K_s)_{\rm Vega}$>2.3]. Finally, we identified star-forming BzK galaxies (BzK-SF) and passively evolving BzK galaxies (BzK-PE) using Equations (2) and (3) in Daddi et al. (2004). In our IRAC selected sample, we identified 6,656 sources as LBGs with R<25.5 (summing up all types), 763 sources as DRGs with K<22.9, and 2,426 as BzK sources with K<22.9 and z>1.4 (summing up the two types).

The average surface density of LBGs with R<25.5 detected by our IRAC survey is 10.0 LBGs/arcmin^2. We detect 0.7 LBGs/arcmin^2 with the GALEX bands and NUV<25.0, a higher density than the one given by Burgarella et al. (2006, 0.3 arcmin^2), but closer to the density given in Burgarella et al. (2007, 1.0 arcmin^2). We find 4.6 LBG-BMs/arcmin^2 (5.3 LBG-BMs/arcmin^2 without any optical magnitude cut), 3.1 LBG-BXs/arcmin^2 (3.6 LBG-BXs/arcmin^2 without any optical magnitude cut), and 1.6 "classical" LBGs/arcmin^2 (2.0 "classical" LBGs/arcmin^2 at any R-magnitude), very similar values to those found in Steidel et al. (2004, 5.3 LBG-BMs/arcmin^2 and 3.6 LBG-BXs/arcmin^2) and Steidel et al. (2003, 1.7 "classical" LBGs/arcmin^2). Adelberger et al. (2004) and Grazian et al. (2007) also find very similar surface densities for the 3 types of LBGs at z>1. The median magnitudes for the LBG sub-sample are R=24.6 and K=23.1, a very faint NIR magnitude only reachable by the deepest ground-based or IRAC surveys. The average photometric redshifts of the different types of LBGs (R<25.5) are: <z>=1.0±0.1 for GALEX LBGs, <z>=1.4±0.3 for LBG-BM (not accounting for the redshift interlopers at z<1, about 17% of all the sources identified as LBG-BM), <z>=2.0±0.4 for LBG-BX (not accounting for the redshift interlopers at z<1, about 34% of all the sources identified as LBG-BX), and <z>=3.1±0.5 for "classical" LBGs. The average spectroscopic redshifts for these types of objects (using the sources where spectroscopy is available) are <z>=1.0±0.2 for GALEX LBGs (spectroscopic redshifts are available for 28% of this sub-sample), <z>=1.4±0.3 for LBGs-BM (spectroscopic redshifts are available for 9% of this sub-sample), <z>=1.7±0.4 for LBGs-BX (using data for 5% of this sub-sample), and <z>=2.5±1.0 for "classical" LBGs (using data for 2% of this sub-sample). The average photometric redshifts are also consistent with the average spectroscopic values published by Steidel et al. (2003) and Steidel et al. (2004), which support the high quality of our photometric redshifts.

The average surface density of DRGs in our IRAC survey is 1.8 DRGs/arcmin^2 (1.1 DRGs/arcmin^2 for sources with K<22.9), a value in between the densities quoted by Franx et al. (2003, 3.0 DRGs/arcmin^2), Förster Schreiber et al. (2004, 1.0–1.6 DRGs/arcmin^2), and Papovich et al. (2006, 0.8 DRGs/arcmin^2). The median magnitudes for the DRG sub-sample are R=25.7 (a very faint optical magnitude beyond the reach of most UV/optical surveys) and K=22.6. The average photometric redshift of the DRGs (K<22.9) is <z>=2.2±1.0, consistent with the values given in Franx et al. (2003) and Papovich et al. (2006). Spectroscopic redshifts are available for just 4% of the DRGs, with an average of <z>=1.5±0.9, a lower value than the photometric estimation, probably due to the bias of spectroscopic surveys towards the optically brightest sources (whose probability of being at lower redshifts is relatively larger).

The average surface density of BzK galaxies at z>1.4 down to K=21.9 is 1.3 BzKs/arcmin^2, divided into 0.2 BzK-PE/arcmin^2 and 1.1 BzK-SF/arcmin^2. This is consistent with the densities given in Daddi et al. (2004, 0.22 BzK-PE/arcmin^2 and 0.91 BzK-SF/arcmin^2) for the same brightness limit. At fainter magnitudes, K<22.9, we identify 0.4 BzK-PE/arcmin^2 and 3.3 BzK-SF/arcmin^2, close to the values found by Reddy

Table 5. The IRAC sample: stellar mass statistics and contribution to the stellar mass density.

Redshift	ALL	Stellar masses[a] and percentage of total stellar mass density											
		LBG				DRG				*BzK*			
	IRAC	Any magnitude		*R*<25.5		Any magnitude		*K*<22.9		Any magnitude		*K*<22.9	
(0.0, 0.2]	$7.4^{8.3}_{6.5}$	$7.2^{8.1}_{6.2}$	12%	$7.4^{8.2}_{6.5}$	12%	$7.7^{8.5}_{7.6}$	0%	$8.3^{8.5}_{7.8}$	0%	$6.6^{7.3}_{5.8}$	1%	$7.3^{8.0}_{6.6}$	1%
(0.2, 0.4]	$8.8^{9.5}_{8.2}$	$8.1^{8.8}_{7.5}$	6%	$8.2^{8.9}_{7.6}$	6%	$8.5^{9.2}_{8.3}$	0%	$8.9^{9.4}_{8.4}$	0%	$7.9^{8.6}_{7.5}$	4%	$8.7^{9.1}_{8.0}$	3%
(0.4, 0.6]	$9.6^{10.1}_{9.1}$	$9.0^{9.3}_{8.7}$	0%	$9.1^{9.3}_{8.8}$	0%	$8.6^{9.7}_{8.4}$	1%	$9.5^{10.0}_{8.5}$	1%	$9.0^{9.3}_{8.4}$	3%	$9.4^{9.7}_{8.6}$	2%
(0.6, 0.8]	$9.7^{10.2}_{9.2}$	$9.1^{9.5}_{8.3}$	5%	$9.2^{9.5}_{8.8}$	5%	$9.7^{10.2}_{8.8}$	1%	$10.1^{10.2}_{9.7}$	0%	$9.1^{9.5}_{8.4}$	6%	$9.7^{10.0}_{9.3}$	6%
(0.8, 1.0]	$9.8^{10.3}_{9.3}$	$9.7^{10.1}_{9.2}$	18%	$9.7^{10.1}_{9.3}$	18%	$9.9^{10.4}_{9.2}$	1%	$10.2^{10.5}_{9.8}$	1%	$9.4^{9.9}_{8.7}$	8%	$10.0^{10.3}_{9.5}$	7%
(1.0, 1.3]	$9.8^{10.3}_{9.4}$	$9.5^{9.9}_{9.1}$	22%	$9.6^{10.0}_{9.2}$	21%	$10.1^{10.6}_{9.5}$	8%	$10.4^{10.7}_{9.9}$	8%	$9.6^{10.1}_{9.1}$	19%	$10.2^{10.5}_{9.8}$	17%
(1.3, 1.6]	$10.2^{10.7}_{9.8}$	$9.9^{10.2}_{9.6}$	24%	$10.0^{10.3}_{9.6}$	23%	$10.7^{11.3}_{10.4}$	7%	$11.0^{11.3}_{10.7}$	7%	$10.2^{10.6}_{9.8}$	72%	$10.6^{10.9}_{10.3}$	67%
(1.6, 2.0]	$10.3^{10.7}_{10.0}$	$10.1^{10.5}_{9.8}$	44%	$10.2^{10.5}_{9.8}$	42%	$10.7^{11.0}_{10.4}$	7%	$10.9^{11.1}_{10.8}$	6%	$10.3^{10.7}_{9.9}$	93%	$10.7^{11.0}_{10.4}$	87%
(2.0, 2.5]	$10.4^{10.9}_{10.0}$	$10.2^{10.6}_{10.0}$	52%	$10.2^{10.6}_{10.0}$	45%	$11.0^{11.2}_{10.7}$	34%	$11.1^{11.3}_{10.9}$	31%	$10.4^{10.9}_{10.0}$	97%	$10.9^{11.2}_{10.6}$	83%
(2.5, 3.0]	$10.4^{10.9}_{10.0}$	$10.3^{10.8}_{9.9}$	45%	$10.3^{10.7}_{9.9}$	34%	$11.0^{11.3}_{10.8}$	63%	$11.2^{11.4}_{11.0}$	53%	$10.5^{11.0}_{10.1}$	87%	$11.0^{11.3}_{10.8}$	69%
(3.0, 3.5]	$10.5^{10.9}_{10.0}$	$10.4^{10.9}_{9.8}$	62%	$10.3^{10.8}_{9.8}$	44%	$11.1^{11.4}_{10.8}$	73%	$11.4^{11.6}_{11.2}$	62%	$10.7^{11.2}_{10.3}$	81%	$11.3^{11.6}_{11.1}$	64%
(3.5, 4.0]	$10.5^{10.9}_{10.0}$	$10.4^{10.8}_{10.0}$	45%	$10.4^{10.7}_{9.9}$	34%	$11.0^{11.3}_{10.7}$	69%	$11.3^{11.5}_{11.1}$	50%	$10.9^{11.3}_{10.6}$	56%	$11.4^{11.6}_{11.1}$	39%

Note. — [a] Logarithms of the median and quartiles of the distribution of stellar masses in units of $[\mathcal{M}_\odot]$.

et al. (2006b, 0.24 *BzK*-PE/arcmin^2 and 3.1 *BzK*-SF/arcmin^2) and Grazian et al. (2007, 0.65 *BzK*-PE/arcmin^2 and 3.2 *BzK*-SF/arcmin^2) for the same magnitude cut. At even fainter K-band magnitudes, the source density of galaxies identified as *BzK* continues rising (especially the SF sub-type) as redshift interlopers become more numerous (up to 40%). The average photometric redshift of *BzK* galaxies (K<22.9) is <z>=2.1±0.7 for *BzK*-PE and <z>=2.0±0.5 for *BzK*-SF (removing the interlopers at z<1.4, a 20% of all *BzK*-PE and 40% of all *BzK*-SF galaxies), again consistent with the literature. Spectroscopic values are <z>=1.7±0.2 (for 1% of *BzK*-PEs) and <z>=1.8±0.5 (using 2% of *BzK*-SFs).

These figures (densities and average redshifts) demonstrate that our IRAC survey constitute an almost complete census of the galaxies at z<4, including most of the LBGs, DRGs, and *BzK* sources, the most important populations of galaxies selected at z>1. Still, some of the IRAC sources are not recovered by any of these selection criteria (even when no magnitude cut is performed for LBGs, DRGs, or *BzK* sources). The numbers of these galaxies just recovered by the deep IRAC observations are given in Table 4.

The LBG population accounts for a negligible fraction (less than 10%) of the entire IRAC sample at 0.4<z<1.0. At z<0.4, ∼30% of IRAC galaxies are classified as LBGs (40% at 0.0<z<0.2 and 20% at 0.2<z<0.4), most of them within the LBG-BX sub-type, which has a significant fraction of z<1 interlopers at bright apparent magnitudes (see Steidel et al. 2004). LBGs selected with GALEX bands are also a minor fraction (around 5%) of the total number of IRAC galaxies at 0.8<z<1.3. However, at z>1, other LBG sub-type start to be very numerous and even dominate the IRAC galaxy counts: ∼35% of all the sources in our IRAC survey at 1.0<z<1.3 are LBGs (80% of them LBG-BMs), 50%–60% at 1.3<z<3.0 (with similar contributions from the different sub-types), 65% at 3.0<z<3.5 (all of them "classical" LBGs), and 50% at 3.5<z<4.0 (all of them "classical" LBGs). These fractions are slightly higher for LBGs not limited by any R-band magnitude.

The median stellar masses of LBGs range from $10^{9.6}$ $\mathcal{M}_\odot$ to $10^{10.2}$ $\mathcal{M}_\odot$ at 1<z<2.5. These values are 0.1–0.2dex lower than the median stellar masses for the global population of IRAC sources at each redshift interval. For this reason, although their numbers are relatively large (even dominate the number counts), LBGs have a less important contribution to the global stellar mass density. Indeed, at 1.0<z<1.6, they harbor less than 25% of the total stellar mass density[7]. At 1.6<z<4.0, they account for 35%–45% of the total stellar mass density (roughly consistent with the estimations from the models in Nagamine et al. 2005b). These percentages increase by 5%–15% if we consider all LBGs without any R-band cut, then making our estimations consistent with those in Grazian et al. (2007, where they do not apply any magnitude cut).

Around 10% of LBGs are detected by MIPS at 24 μm above the 75% completeness flux level (20% with any flux), especially at 1.6<z<2.5, where MIPS is more efficient detecting sources due to the pass of the 7.7 μm PAH feature through the filter. At z>2.5, the fraction of MIPS detections is about 10%, consistent with Huang et al. (2005). MIPS detections are more common for the highest mass galaxies: the median stellar mass for 24 μm detected LBGs ($10^{10.9}$ $\mathcal{M}_\odot$ at z∼2.5 and $10^{11.1}$ $\mathcal{M}_\odot$ at z∼3.0 for sources with $F(24)$=80 μJy) is ∼0.8dex larger than the median for all LBGs. LBGs with MIPS detections account for 10%–20% of the total stellar mass at z>1.5.

In contrast with the previous figures for LBGs, DRGs are less numerous but more massive. DRGs only account for 15% of the sources at 2.0<z<2.5, and ∼30% at 2.5<z<4.0. However, their median stellar masses are larger than those of LBGs at each redshift, and

[7] This percentage has been calculated by adding the total stellar masses of LBGs in that redshift interval, and dividing it by the total stellar masses of all galaxies. This must be analogous to dividing the stellar mass densities of both galaxy populations for a fixed volume (that enclosed at the given redshift interval).

even larger than the median for the entire population of IRAC sources. For 1<z<2, their median masses are 0.3-0.5dex larger than those for the entire IRAC population, and at z>2 they remain ∼0.6dex larger (with a median of $10^{11.0}$ $\mathcal{M}_{\odot}$). This translates to DRGs accounting for 70% of the total stellar mass at z>2.5 (∼35% at 2.0<z<2.5, and less than 10% below z=2). Note that most of the stellar mass density of the Universe at z>2.5 would not be detected by optical surveys reaching depths brighter than R∼25.5. Within the DRG population, about 40% are detected by MIPS at 24 μm (up to 50% at 2.0<z<3.5), and these objects have median stellar masses 0.1-0.3dex larger than the median for all DRGs. DRGs with MIPS detections account for more than 40% of the total stellar mass at z>2.5 (20% at 2.0<z<2.5, and less than 5% at z<2.0) .

The BzK criterium is very effective in detecting massive galaxies at z>1.5, even more than the $J-K$ selection of DRGs. Up to 75%–95% of the IRAC sources at 1.3<z<2.5 are recovered by the BzK selection, 80% at 2.5<z<3.0, 55% at 3.0<z<3.5, and 30% beyond z=3.5. If we only consider BzK galaxies with K<22.9, these percentages decrease by a factor of ∼2. Most of the BzK galaxies are classified as star-forming (typically 90%). Median masses for BzK galaxies range from $10^{10.2}$ at z=1.5 to $10^{10.6}$ at z=3.0 and $10^{10.9}$ at z=4.0, 0.1–0.4 dex larger than median stellar masses for the whole IRAC sample. This translates into BzK galaxies tracing a large fraction of the stellar mass density at z>1.5: more than 55% and up to 97% at z>1.3. Again, if we only consider BzK galaxies with K<22.9, these percentages decrease by 15%-20%. Typically, 30% or more BzK galaxies are detected by MIPS at 24 μm, with a predilection for the passively evolving sub-type at z>2 (∼60% ∼30% of BzK-PE and BzK-SF galaxies are detected by MIPS). This means that passively evolving BzK galaxies may still harbor significant star formation or obscured AGNs.

Very few galaxies are identified as LBGs and DRGs simultaneously in our IRAC survey: just 5% of all galaxies at 2.0<z<3.0, ∼8% at z>3, and less than 1% elsewhere. However, this does not mean that the 2 selection criteria are completely orthogonal. Indeed, about 20% of the DRGs at z=2–3 and 30% of the DRGs at z>3 qualify as LBGs, and 15% of LBGs at z>2.5 are DRGs. Most of the LBGs that also qualify as DRGs lie in the "classical" subtype (more than 95% of them), which makes our results also consistent with the fractions found in Grazian et al. (2007), who only discussed BM-BX objects. Note that if we only consider the DRGs brighter than K=21.9, the fraction of LBGs that are also DRGs drops below the 5% level, in good agreement with the 10% upper limit prediction from the hydrodynamic models of Nagamine et al. (2005a).

The BzK and DRG selection criteria present a large overlap. Around 20%–30% of all IRAC galaxies at z>2 are recovered by both selection techniques, especially by the BzK-SF criterium. Indeed, more than 95% of all DRGs at 1.5<z<3.0 are BzK galaxies, most of them (∼90%) within the star-forming BzK sub-type. DRGs are only a minor contributor to the BzK population at z<3, where less than 35% of BzK sources are DRGs, but this percentage rises to 70% at z>3.5. It is also interesting to mention that 50% of BzK-PE galaxies at 2.0<z<2.5 and all the BzK-PE galaxies at z>2.5 are DRGs.

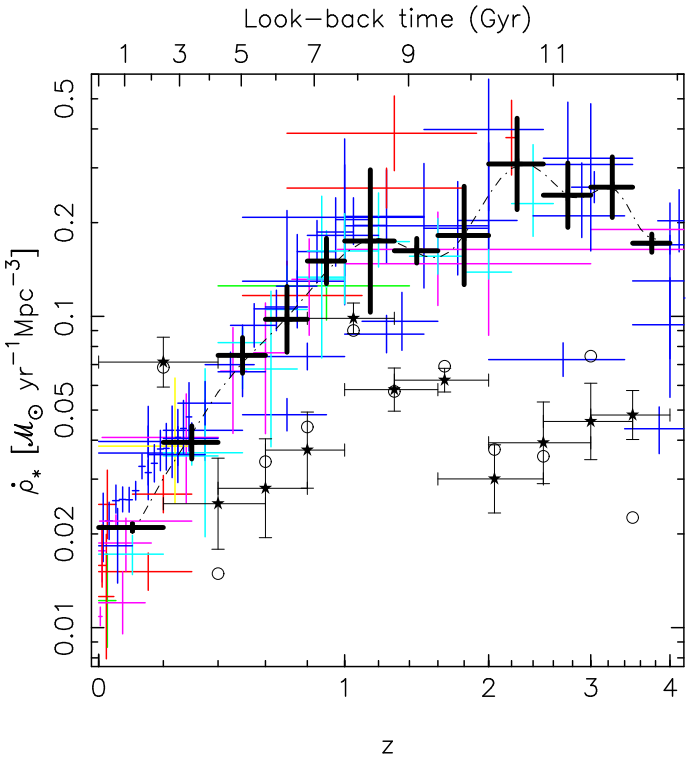

FIG. 9.— Evolution of the co-moving SFR density of the Universe (Lilly-Madau plot, Lilly et al. 1996; Madau et al. 1996). Filled stars and thin error bars show the SFR density estimations based on the time derivative of the stellar mass density evolution shown in Figure 7. Open circles show the derivative for the observed values of the stellar mass density. The colored points (shown with error bars) are extracted from different sources in the literature (using different SFR tracers), normalized to the same cosmology by Hopkins (2004) and Hopkins & Beacom (2006). Red symbols are estimations based on Hydrogen emission-lines, and green points on $[OII]\lambda3737$ SFR estimations. UV-based data points are plotted in blue. Cyan estimations are based on mid-infrared data. Magenta points are based on sub-mm and radio observations. The yellow point is based on X-ray data. Thick black error bars show weighted averages and standard deviations of the literature data points for the 12 redshift intervals considered for the stellar mass functions in this paper. These averages are fitted to a Chebyshev polynomial of 13^{th} order (dash-dotted line).

None of the LBGs lie in the BzK-PE type, but the BzK-SF type also has a large overlap with the LBG population: more than 95% of BM-BX galaxies up to z>2 are recovered in the BzK diagram (consistent with Reddy et al. 2005), and less than 40% in the case of "classical" LBGs at z>3.

7. LINKING STELLAR MASSES AND STAR FORMATION RATES UP TO z=4

7.1. *The evolution of the cosmic star formation rate density*

The time derivative of the stellar mass density function plotted in Figure 7 gives the evolution of the SFR density of the Universe, i.e., the well-known Lilly-Madau plot (Lilly et al. 1996; Madau et al. 1996). For each pair of stellar mass density points in Figure 7, we have estimated the SFR (averaged through the time interval enclosed by the points) necessary to produce the stellar

mass density difference between the corresponding redshifts. These estimations are plotted in Figure 9 with filled black stars (open circles show the average SFRs derived from the observed stellar mass density values), and compared with other cosmic SFR density estimations (based on direct SFR measurements) found in the literature. Surprisingly, our estimations of the cosmic SFR density are systematically smaller than the previously published results (a factor of ∼2 at z<1 and up to a factor of 10 at high redshift). This important discrepancy has also been remarked by Hopkins & Beacom (2006) and Borch et al. (2006), who integrate the time evolution of the cosmic SFR density to obtain the evolution of the stellar mass density. Hopkins & Beacom (2006) argue that the difference can be related to a limitation in our understanding of the IMF, given that the direct SFR estimations are sensitive to the high mass end of the IMF, while the stellar mass estimations are sensitive to the low mass end. The origin of the discrepancy can also be linked to the way we estimate SFR densities. In our case, we assumed that star formation occurred at a constant rate within a redshift (time) interval in Figure 7, and calculated an average SFR density. However, if star formation occurs in very short episodes (very different from a constant rate), one could measure SFRs for each galaxy that are larger than the constant rate, but still produce the same amount of stars in the same time interval. If this interpretation is right, then the star formation at the highest redshifts should occur in very intense and rapid events, since the difference between the literature data points and our average SFR densities are larger than at low redshift. Finally, the reader should also note the very high SFR density derived for 0.0<z<0.4 from the stellar mass density derivative, directly related to the significant increase in the stellar mass density of the Universe in this time period, as discussed in previous Sections. Direct SFR density measurements at z<0.4 are a factor of 2–4 smaller, which indicates that the evolution of the stellar mass function at low redshift is not governed by star formation (but by mergers) and/or we may be underestimating the stellar mass density at z∼0.4 (if there is a numerous population of low mass galaxies below our detection limit, which can merge together in the last 4 Gyr to increase the density of galaxies with mass $\mathcal{M}$=10^{9-11} $\mathcal{M}_{\odot}$) or overestimating the local value.

7.2. *Specific star formation rates*

Figure 10 shows the evolution of the specific SFR (SFR per stellar mass unit) of the Universe, calculated by dividing the Chebyshev fit to the cosmic SFR density (given in Figure 9[8]) by the Chebyshev fit to the stellar mass evolution (given in Figure 7). There is a continuous increase of the specific SFR of the Universe as we move to higher redshifts. If we consider the evolution of the specific SFR for different stellar mass intervals (color lines in Figure 10), we clearly see that the most massive galaxies ($\mathcal{M}$>$10^{11.7}$ $\mathcal{M}_{\odot}$) presented very large specific SFRs at high redshift. These galaxies exhibit values of the SFR that are so large that they could double their stellar mass in just 0.1 Gyr (see the scale on the left axis) at z=3–4. As we move to lower redshifts, their specific SFRs decrease considerably, by a factor of 10 from z∼4 to z∼2.5 (in less than 1.5 Gyr), and by almost a factor of 100 from z∼4 to z∼1.5 (in 3 Gyr). For lower stellar masses, the evolution is less pronounced. For example, galaxies with $10^{10.0}$<$\mathcal{M}$<$10^{11.0}$ $\mathcal{M}_{\odot}$, whose evolution is very similar to the cosmic average, present a decrease in the specific SFR of a factor of 10 from z∼2.5 to z∼0.5 (in 6 Gyr). The evolution at z<1 is very similar for all the stellar mass intervals, as already noted by Zheng et al. (2007), with a change of about a factor of 10 in this period of ∼8 Gyr. In this period, there is a significant luminosity (and maybe density) evolution of luminous IR galaxies (Chary & Elbaz 2001; Pérez-González et al. 2005). This evolution is also detected in our stellar mass analysis, given that the fraction of the total stellar mass density locked in galaxies emitting strongly in the thermal IR (and being detected by MIPS) increase from about 10% at z=0 to ∼50% at z=0.7–1.0 (where LIRGs dominate the cosmic SFR density), and then remains approximately constant up to z=4 (where LIRGs and even ULIRGs dominate the SFR density).

The evolution of the cosmic specific SFR is also con-

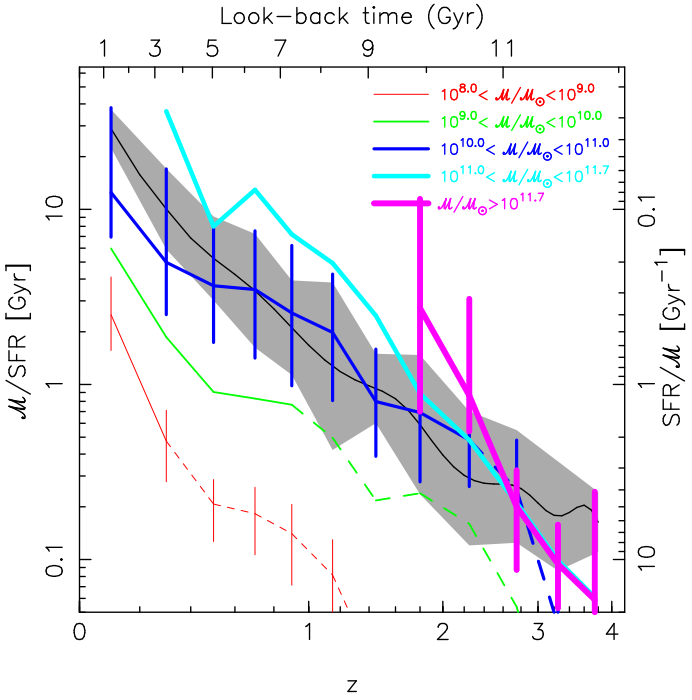

FIG. 10.— Evolution of the cosmic specific SFR. The black continuous line shows the evolution derived from the Chebyshev fits to the SFR and stellar mass density evolution plotted in Figures 7 and 9. The gray shaded area depicts the typical uncertainties in the calculation of the cosmic specific SFR. Color lines join the median values of the distribution of specific SFRs of our IRAC sample for several mass intervals, while vertical error bars show the quartiles of that distribution. For clarity, we have only depicted the quartiles for non-consecutive mass intervals. We only show the median and quartiles for redshift bins where we detect more than 10 galaxies within a given stellar mass interval. Dashed lines mark the redshift ranges where our sample is less than 75% complete for the given mass interval.

[8] The coefficients of the Chebyshev polynomial fit (with variable 1+z) to the SFR density evolution are [0.3267, 0.0818, −0.0772, −0.0140, 0.0043, 0.0114, 0.0043, −0.0091, 0.0072, 0.0135, −0.0091, −0.0134, 0.0048].

sistent with the "downsizing" picture described in Section 5 5.6, where the most massive galaxies formed most of their mass at z>3 in very intense and rapid episodes of star formation, presenting high specific SFRs which would double the stellar mass of these systems in time scales shorter than 1 Gyr. Less massive systems assembled more slowly, presenting specific SFRs which would double their mass in time scales comparable to the look-back time of the Universe at each redshift.

8. CONCLUSIONS

We characterize the mass assembly of galaxies in the last 12 Gyr (∼90% of the Hubble time) by analyzing the stellar mass functions and densities estimated from a sample of ∼28,000 sources selected in the rest-frame near-infrared. The sample has been built from *Spitzer*/IRAC (the selection being made at 3.6 μm and 4.5 μm) observations of 3 fields: the Hubble Deep Field North, the Chandra Deep Field South, and the Lockman Hole. This IRAC sample is 75% complete down to 1.6 μJy ([3.6]=23.4), which translates to an approximate stellar mass completeness level of at least 10^9 $\mathcal{M}_\odot$ up to z=0.5, 10^{10} $\mathcal{M}_\odot$ up to z=1.0, and 10^{11} $\mathcal{M}_\odot$ up to z=4.0. In order to analyze the effects on our results of low mass galaxies faint at rest-frame near-infrared wavelengths, we complement the IRAC survey with an optically (I<25.5) selected sample of a similar size.

We estimate photometric redshifts, stellar masses, and star formation rates for all galaxies using a set of empirical templates built by modelling the stellar population and dust emission of galaxies with known spectroscopic redshifts. The quality of our photometric redshifts is very good for more than 85% of the sample, and good for nearly 95%. We analyze the goodness of the stellar mass and star formation rate estimates, finding that they are accurate within a factor of 2–3.

Our estimation of the local stellar mass function is in good agreement with previous estimations based on 2MASS data (Bell et al. 2003; Cole et al. 2001). We find a slope of $\alpha\sim$–1.2 at low stellar masses (similar values are also found for stellar mass functions at all redshifts up to z=4), and a pronounced steepening of the stellar mass function at $\mathcal{M}<10^9$ $\mathcal{M}_\odot$. Approximately 1 out of 4 local galaxies are actively forming stars. Around 10–15% of the global stellar mass density in the local Universe is found in active star-forming galaxies (in agreement with Pérez-González et al. 2003a), and this percentage rises to ∼50% at z∼1, remaining approximately constant beyond that redshift.

Our results indicate that the most massive systems ($\mathcal{M}>10^{12.0}$ $\mathcal{M}_\odot$) assembled the bulk of their stellar mass in a very rapid collapse (half of their stellar mass in less than 1 Gyr) at early epochs (z>3 or 11 Gyr ago), close to what can be regarded as a monolithic collapse. The formation was characterized by large specific SFRs with doubling times of about 0.1 Gyr. Galaxies with $10^{11.5}<\mathcal{M}<10^{12.0}$ $\mathcal{M}_\odot$ formed more slowly, assembling half of their stellar mass before z∼1.5 (more than 9 Gyr ago) and more than 90% of their stellar mass beyond z∼0.6. Less massive systems (with $10^{9.0}<\mathcal{M}<10^{11.0}$ $\mathcal{M}_\odot$) formed at even a slower speed: half of their stellar mass was assembled beyond z∼1 (more than 7 Gyr ago), and they experienced a significant increase in their stellar mass (20%–40%) recently (at z<0.4 or in the last 3 Gyr), probably by dry accretion of small satellite galaxies. The specific SFRs of these galaxies evolved (closely to the cosmic average) from 10 Gyr^{-1} at z∼4 to less than 0.1 Gyr^{-1} in the local Universe.

We find that approximately half of the local stellar mass density was already formed at z∼1 (8 Gyr ago), which translates to an average assembling rate of 0.036 $\mathcal{M}_\odot$yr^{-1}. At least another 40% of the local stellar mass density assembled from z=1 to z=4 (in 4 Gyr) at an average rate of 0.054 $\mathcal{M}_\odot$yr^{-1}.

We confirm that galaxy formation follows a "downsizing" scenario (Cowie et al. 1996). Our results are broadly consistent with previous observational works that confirm this formation theory (Fontana et al. 2006; Glazebrook et al. 2004; Heavens et al. 2004; Juneau et al. 2005; Pérez-González et al. 2005), and with models of galaxy formation (e.g., Bower et al. 2006; Croton et al. 2006; Nagamine et al. 2004). At low redshift (z<1), there is also an "upsizing" effect, when intermediate mass galaxies ($\mathcal{M}=10^{9-11}$ $\mathcal{M}_\odot$) increase their density by accretion or coalescence of previously formed smaller galaxies.

We have also analyzed the nature of the galaxies in our sample, comparing them with the populations of sources detected with different selection techniques by other surveys. Based on the measured number densities and redshifts, we conclude that our survey constitutes an almost complete census of the different populations of galaxies at high redshifts, including most of the Lyman Break Galaxies (LBGs) at 1<z<3.5, most of the Distant Red Galaxies (DRGs) at z$\gtrsim$2, and most of the BzK galaxies at z>1.4. LBGs dominate the number counts of IRAC galaxies at high redshift, being about a factor of 2–3 more numerous than DRGs and BzK galaxies, but most of the stellar mass density (more than 50% and up to 97%) at z>2.5 resides in the latter, while LBGs account for less than 50% of the total stellar mass density.

We acknowledge support from the Spanish Programa Nacional de Astronomía y Astrofísica under grant AYA 2006–02358. Support was also provided by NASA through Contract no. 1255094 issued by JPL/Caltech. This work is based in part on observations made with the *Spitzer* Space Telescope, which is operated by the Jet Propulsion Laboratory, Caltech under NASA contract 1407. GALEX is a NASA Small Explorer launched in 2003 April. We gratefully acknowledge NASA's support for construction, operation, and scientific analysis of the GALEX mission. This research has made use of the NASA/IPAC Extragalactic Database (NED) which is operated by the Jet Propulsion Laboratory, California Institute of Technology, under contract with the National Aeronautics and Space Administration. Based in part on data collected at Subaru Telescope and obtained from the SMOKA, which is operated by the Astronomy Data Center, National Astronomical Observatory of Japan. PGP-G acknowledges support from the Ramón y Cajal Fellowship Program financed by the Spanish Government, and AGdP from the MAGPOP EU Marie Curie Research Training Network. We are grateful to Andrew Hopkins for providing useful data for this paper.

REFERENCES

Abraham et al. 2006, ApJ (submitted), astro-ph/0701779
Adelberger, K. L., Steidel, C. C., Shapley, A. E., Hunt, M. P., Erb, D. K., Reddy, N. A., & Pettini, M. 2004, ApJ, 607, 226
Alonso-Herrero, A., Rieke, G. H., Rieke, M. J., Colina, L., Pérez-González, P. G., & Ryder, S. D. 2006, ApJ, 650, 835
Arendt, R. G. et al. 1998, ApJ, 508, 74
Baldry, I. K., & Glazebrook, K. 2003, ApJ, 593, 258
Bauer, A. E., Drory, N., Hill, G. J., & Feulner, G. 2005, ApJ, 621, L89
Baugh, C. M., Cole, S., Frenk, C. S., & Lacey, C. G. 1998, ApJ, 498, 504
Baugh, C. M., Lacey, C. G., Frenk, C. S., Granato, G. L., Silva, L., Bressan, A., Benson, A. J., & Cole, S. 2005, MNRAS, 356, 1191
Bell, E. F., McIntosh, D. H., Katz, N., & Weinberg, M. D. 2003, ApJS, 149, 289
Bell, E. F. et al. 2005, ApJ, 625, 23
Benítez, N. 2000, ApJ, 536, 571
Bertin, E., & Arnouts, S. 1996, A&AS, 117, 393
Blain, A. W., Smail, I., Ivison, R. J., Kneib, J.-P., & Frayer, D. T. 2002, Phys. Rep., 369, 111
Bolzonella, M., Miralles, J.-M., & Pelló, R. 2000, A&A, 363, 476
Borch, A. et al. 2006, A&A, 453, 869
Bower, R. G., Benson, A. J., Malbon, R., Helly, J. C., Frenk, C. S., Baugh, C. M., Cole, S., & Lacey, C. G. 2006, MNRAS, 370, 645
Brinchmann, J., & Ellis, R. S. 2000, ApJ, 536, L77
Brocklehurst, M. 1971, MNRAS, 153, 471
Brown, M. J. I., Dey, A., Jannuzi, B. T., Brand, K., Benson, A. J., Brodwin, M., Croton, D. J., & Eisenhardt, P. R. 2007, ApJ, 654, 858
Bruzual, G. 2007, astro-ph/0702091
Bruzual, G., & Charlot, S. 2003, MNRAS, 344, 1000
Bundy, K. et al. 2006, ApJ, 651, 120
Burgarella, D., Le Floc'h, E., Takeuchi, T. T., Buat, V., Huang, J. S., Rieke, G. H., & Tyler, K. D. 2007, astro-ph/0701322
Burgarella, D. et al. 2006, A&A, 450, 69
Calzetti, D., Armus, L., Bohlin, R. C., Kinney, A. L., Koornneef, J., & Storchi-Bergmann, T. 2000, ApJ, 533, 682
Caputi, K. I. et al. 2006, ApJ, 637, 727
Charlot, S., & Fall, S. M. 2000, ApJ, 539, 718
Chary, R., & Elbaz, D. 2001, ApJ, 556, 562
Chen, H. et al. 2003, ApJ, 586, 745
Cole, S., Lacey, C. G., Baugh, C. M., & Frenk, C. S. 2000, MNRAS, 319, 168
Cole, S. et al. 2001, MNRAS, 326, 255
Conselice, C. J., Blackburne, J. A., & Papovich, C. 2005, ApJ, 620, 564
Cowie, L. L., Barger, A. J., Hu, E. M., Capak, P., & Songaila, A. 2004, AJ, 127, 3137
Cowie, L. L., Songaila, A., Hu, E. M., & Cohen, J. G. 1996, AJ, 112, 839
Croton, D. J. et al. 2006, MNRAS, 365, 11
Daddi, E., Cimatti, A., Renzini, A., Fontana, A., Mignoli, M., Pozzetti, L., Tozzi, P., & Zamorani, G. 2004, ApJ, 617, 746
Dale, D. A., & Helou, G. 2002, ApJ, 576, 159
De Lucia, G., Springel, V., White, S. D. M., Croton, D., & Kauffmann, G. 2006, MNRAS, 366, 499
Dey, A., Graham, J. R., Ivison, R. J., Smail, I., Wright, G. S., & Liu, M. C. 1999, ApJ, 519, 610
Dickinson, M., Giavalisco, M., & The Goods Team. 2003a, in The Mass of Galaxies at Low and High Redshift, ed. R. Bender & A. Renzini, 324
Dickinson, M. et al. 2000, ApJ, 531, 624
Dickinson, M., Papovich, C., Ferguson, H. C., & Budavári, T. 2003b, ApJ, 587, 25
Drory, N., Bender, R., Feulner, G., Hopp, U., Maraston, C., Snigula, J., & Hill, G. J. 2004, ApJ, 608, 742
Drory, N., Salvato, M., Gabasch, A., Bender, R., Hopp, U., Feulner, G., & Pannella, M. 2005, ApJ, 619, L131
Efstathiou, G., Ellis, R. S., & Peterson, B. A. 1988, MNRAS, 232, 431
Eisenhardt, P. R. et al. 2004, ApJS, 154, 48
Elston, R., Rieke, G. H., & Rieke, M. J. 1988, ApJ, 331, L77
Fazio, G. G. et al. 2004a, ApJS, 154, 39
—. 2004b, ApJS, 154, 10
Ferland, G. J. 1980, PASP, 92, 596
Fioc, M., & Rocca-Volmerange, B. 1997, A&A, 326, 950
Fontana, A. et al. 2003, ApJ, 594, L9
—. 2004, A&A, 424, 23
—. 2006, A&A, 459, 745
Förster Schreiber, N. M. et al. 2004, ApJ, 616, 40
Franx, M. et al. 2003, ApJ, 587, L79
Gil de Paz, A., & Madore, B. F. 2002, AJ, 123, 1864
Glazebrook, K. et al. 2004, Nature, 430, 181
Granato, G. L., De Zotti, G., Silva, L., Bressan, A., & Danese, L. 2004, ApJ, 600, 580
Grazian, A. et al. 2006, A&A, 449, 951
Grazian, A., Nonino, M., & Gallozzi, S. 2007, astro-ph/0701233
Heavens, A., Panter, B., Jimenez, R., & Dunlop, J. 2004, Nature, 428, 625
Hopkins, A. M. 2004, ApJ, 615, 209
Hopkins, A. M., & Beacom, J. F. 2006, ApJ, 651, 142
Huang, J.-S. et al. 2005, ApJ, 634, 137
Hughes, D. H. et al. 1998, Nature, 394, 241
Im, M., Yamada, T., Tanaka, I., & Kajisawa, M. 2002, ApJ, 578, L19
Jimenez, R., Bernardi, M., Haiman, Z., Panter, B., & Heavens, A. F. 2006, ApJ (submitted), astro-ph/0610724
Juneau, S. et al. 2005, ApJ, 619, L135
Kauffmann, G. et al. 2003, MNRAS, 341, 33
Kauffmann, G., White, S. D. M., & Guiderdoni, B. 1993, MNRAS, 264, 201
Kennicutt, R. C. 1998, ARA&A, 36, 189
Kron, R. G. 1980, ApJS, 43, 305
Kroupa, P., Tout, C. A., & Gilmore, G. 1993, MNRAS, 262, 545
Le Fèvre, O. et al. 2004, A&A, 428, 1043
Le Floc'h, E. et al. 2005, ApJ, 632, 169
Lilly, S. J., Le Fevre, O., Hammer, F., & Crampton, D. 1996, ApJ, 460, L1
Loveday, J. 2000, MNRAS, 312, 557
Madau, P., Ferguson, H. C., Dickinson, M. E., Giavalisco, M., Steidel, C. C., & Fruchter, A. 1996, MNRAS, 283, 1388
Mainieri, V., Bergeron, J., Rosati, P., Hasinger, G., & Lehmann, I. 2002, astro-ph/0202211
Maraston, C. 2005, MNRAS, 362, 799
Nagamine, K., Cen, R., Hernquist, L., Ostriker, J. P., & Springel, V. 2004, ApJ, 610, 45
—. 2005a, ApJ, 627, 608
—. 2005b, ApJ, 618, 23
Nagamine, K., Ostriker, J. P., Fukugita, M., & Cen, R. 2006, ApJ, 653, 881
Osterbrock, D. E. 1989, Astrophysics of gaseous nebulae and active galactic nuclei (Research supported by the University of California, John Simon Guggenheim Memorial Foundation, University of Minnesota, et al. Mill Valley, CA, University Science Books, 1989, 422 p.)
Pérez-González, P. G., Gallego, J., Zamorano, J., Alonso-Herrero, A., Gil de Paz, A., & Aragón-Salamanca, A. 2003a, ApJ, 587, L27
Pérez-González, P. G., Gallego, J., Zamorano, J., & Gil de Paz, A. 2001, A&A, 365, 370
Pérez-González, P. G., Gil de Paz, A., Zamorano, J., Gallego, J., Alonso-Herrero, A., & Aragón-Salamanca, A. 2003b, MNRAS, 338, 508
—. 2003c, MNRAS, 338, 525
Pérez-González, P. G. et al. 2005, ApJ, 630, 82
Pannella, M., Hopp, U., Saglia, R. P., Bender, R., Drory, N., Salvato, M., Gabasch, A., & Feulner, G. 2006, ApJ, 639, L1
Papovich, C., & Bell, E. F. 2002, ApJ, 579, L1
Papovich, C. et al. 2006, ApJ, 640, 92
Reddy, N. A., Erb, D. K., Steidel, C. C., Shapley, A. E., Adelberger, K. L., & Pettini, M. 2005, ApJ, 633, 748
Reddy, N. A., Steidel, C. C., Erb, D. K., Shapley, A. E., & Pettini, M. 2006a, ApJ, 653, 1004
Reddy, N. A., Steidel, C. C., Fadda, D., Yan, L., Pettini, M., Shapley, A. E., Erb, D. K., & Adelberger, K. L. 2006b, ApJ, 644, 792
Rowan-Robinson, M. et al. 2005, AJ, 129, 1183

Salpeter, E. E. 1955, ApJ, 121, 161
Salucci, P., & Persic, M. 1999, MNRAS, 309, 923
Schechter, P. 1976, ApJ, 203, 297
Schiminovich, D. et al. 2005, ApJ, 619, L47
Smail, I., Ivison, R. J., & Blain, A. W. 1997, ApJ, 490, L5
Somerville, R. S., Primack, J. R., & Faber, S. M. 2001, MNRAS, 320, 504
Steidel, C. C., Adelberger, K. L., Shapley, A. E., Pettini, M., Dickinson, M., & Giavalisco, M. 2003, ApJ, 592, 728
Steidel, C. C., Shapley, A. E., Pettini, M., Adelberger, K. L., Erb, D. K., Reddy, N. A., & Hunt, M. P. 2004, ApJ, 604, 534
Szokoly, G. P. et al. 2004, ApJS, 155, 271
Tresse et al. 2006, A&A (submitted), astro-ph/060900
Treu, T. et al. 2005, ApJ, 633, 174
van der Wel, A., Franx, M., van Dokkum, P. G., Rix, H.-W., Illingworth, G. D., & Rosati, P. 2005, ApJ, 631, 145
van Dokkum, P. G. et al. 2003, ApJ, 587, L83
Vanzella, E. et al. 2005, A&A, 434, 53
—. 2006, A&A, 454, 423
Wainscoat, R. J., Cohen, M., Volk, K., Walker, H. J., & Schwartz, D. E. 1992, ApJS, 83, 111
Werner, M. W. et al. 2004, ApJS, 154, 1
Willmer, C. N. A. 1997, AJ, 114, 898
Wirth, G. D. et al. 2004, AJ, 127, 3121
Yan, L., McCarthy, P. J., Weymann, R. J., Malkan, M. A., Teplitz, H. I., Storrie-Lombardi, L. J., Smith, M., & Dressler, A. 2000, AJ, 120, 575
Zappacosta, L., Maiolino, R., Finoguenov, A., Mannucci, F., Gilli, R., & Ferrara, A. 2005, A&A, 434, 801
Zheng, X. Z., Bell, E. F., Papovich, C., Wolf, C., Meisenheimer, K., Rix, H.-W., Rieke, G. H., & Somerville, R. 2007, astro-ph/0702208